

The Structures of Distant Galaxies I: Galaxy Structures and the Merger Rate to $z \sim 3$ in the Hubble Ultra-Deep Field

Christopher J. Conselice^{1*}, Sheena Rajgor¹, Robert Myers¹

¹*University of Nottingham, School of Physics & Astronomy, Nottingham, NG7 2RD UK*

Accepted ; Received ; in original form

ABSTRACT

This paper begins a series in which we examine the structures of distant galaxies to directly determine the history of their formation modes. We start this series by examining the structures of $z_{F850LP} < 27$ galaxies in the Hubble Ultra-Deep field, the deepest high-resolution optical image taken to date. We investigate a few basic features of galaxy structure using this image. These include: (1) The agreement of visual eye-ball classifications and non-parametric quantitative (CAS, Gini/ M_{20}) methods; (2) How distant galaxy quantitative structures can vary as a function of rest-frame wavelength; and (3) The evolution of distant galaxy structures up to $z \sim 3$. One of our major conclusions is that the majority of galaxies with $z_{850} < 27$ are peculiar in appearance, and that galaxy assembly is rapidly occurring at these magnitudes, even up to the present time. We find a general agreement between galaxy classification by eye and through quantitative methods, as well as a general agreement between the CAS and the Gini/ M_{20} parameters. We find that the Gini/ M_{20} method appears to find a larger number of galaxy mergers than the CAS system, but contains a larger contamination from non-mergers. We furthermore calculate the merger rate of galaxies in the UDF up to $z \sim 3$, finding an increase with redshift as well as stellar mass, confirming previous work in the Hubble Deep Field. We find that massive galaxies with $M_* > 10^{10} M_{\odot}$ undergo $4.3_{+0.8}^{-0.8}$ major galaxy mergers at $z < 3$, with all of this merging occurring at $z > 1$.

Key words: Galaxies: Evolution, Formation, Structure, Morphology, Classification

1 INTRODUCTION

Understanding the formation of galaxies is one of the most intriguing and unanswered problems in astronomy today. Studying galaxies in the distant universe is one of the major approaches for deciphering their formation and evolution. Traditionally, distant galaxies are examined in terms of their gross properties, such as luminosities (e.g., Faber et al. 2007), colours (e.g., Moustakas et al. 2004), and sizes (Trujillo et al. 2007), and stellar masses (e.g., Bundy et al. 2005; Conselice et al. 2007a,b). The least developed approached, but potentially one of the most exciting for revealing unique information, is how the structures and morphologies of galaxies change through cosmic time.

The reason a structural and morphological approach is potentially the most fruitful for understanding galaxy formation and evolution is that the structures of galaxies cor-

relate with formation modes, such as star formation and galaxy mergers (Conselice 2003). It is thus possible to determine the physical processes behind galaxy formation directly without having to compare observables with physical models. This direct approach has been used in the past to calculate the role of galaxy mergers in the formation of massive galaxies (e.g., Conselice et al. 2003a; Lotz et al. 2006; Conselice 2006). This previous work showed that the most massive galaxies with $M_* > 10^{10} M_{\odot}$ appear to form nearly all their stellar mass in mergers, which occur mostly, and in large numbers, at $z > 1.5$.

There are however still many outstanding problems with using galaxy structure to derive evolution, including the reliability of the approaches used, and the uniqueness and repeatability of results thus far obtained. For the most part, it is necessary to use deep Hubble Space Telescope imaging to measure the structures and morphologies of a large number of distant galaxies, although adaptive optics, particularly in the near-infrared, is becoming another pow-

* E-mail: conselice@nottingham.ac.uk

erful approach (e.g., Wright et al. 2007). Since the imaging cameras on the Hubble Space Telescope are limited in field of view, only a small fraction of distant galaxies have been studied thus far (e.g., Williams et al. 1996; Giavalisco et al. 2004). Particularly, most of the merger history of galaxies at $z > 1$ has been measured within the Hubble Deep Field-North, which currently has the only high resolution deep near-infrared imaging of distant galaxies (e.g., Dickinson et al. 2000; Conselice et al. 2003a; Papovich et al. 2005). Thus, it is important to study the structures and morphologies of galaxies in as many fields as possible, using different techniques.

The Hubble Ultra Deep Field (UDF) represents perhaps our best opportunity to study the most distant galaxies at observed optical wavelengths for the foreseeable future. The UDF is a major Hubble imaging program utilising the Advanced Camera for Surveys (ACS) to image a single pointing in the sky to the deepest depth ever probed in the optical. As the ACS UDF images are very deep, and have a higher resolution than the WFPC2 HDFs, we can address some fundamental questions concerning galaxy structure and morphology. These include: understanding the nature of galaxy morphologies seen in deep optical surveys; the agreement, or lack thereof, between apparent morphology and structural parameters; and the evolution of galaxy structure through time. We are particularly interested in determine how major galaxy mergers are driving the formation of the galaxy population at early times.

Our major finding in this paper is that galaxies in the past are significantly more irregular, peculiar, asymmetric, and clumpy than galaxies today, and that this likely results from the past merger and assembly activity that established these systems. We show that a large fraction of this irregularity cannot be produced simply by star formation, and derive the merger fraction and rate for galaxies of various stellar masses. We confirm the findings of Conselice et al. (2003a) and Conselice (2006) that massive galaxies with $M_* > 10^{10} M_\odot$ have a steeply increasing merger fraction, which evolves as $\sim (1+z)^6$ between $z = 0.8$ and 3. This suggests that these massive galaxies undergo on average $4.3^{+0.8}_{-0.8}$ major mergers between $z \sim 3$ to 0.

This paper is organised as follows: §2 includes a discussion of the data sources we use in this paper, §3 is a description of our morphological and structural analyses, and the stellar masses we utilise, §4 is a discussion of our results, including how different structural analysis techniques compare with each other, especially how merger finding methods differ, §5 gives our description of the merger history up to $z \sim 3$, and §6 is our summary and conclusions. We use a standard cosmology of $H_0 = 70 \text{ km s}^{-1} \text{ Mpc}^{-1}$, and $\Omega_m = 1 - \Omega_\lambda = 0.3$ throughout.

2 DATA AND DATA SOURCES

The primary data source used in this paper are the ACS and NICMOS imaging of the Hubble Ultra Deep Field (Thompson et al. 2005; Beckwith et al. 2006). The field of view of the ACS image is 11 arcmin^2 , and is located within the GOODS-South field (Giavalisco et al. 2004). The UDF ACS images use the same filter set as the GOODS data, which are the F435W (B₄₃₅), F606W (V₆₀₆), F775W (i₇₇₅), and F850L

(z₈₁₅) bands. The central wavelengths of these filters, and their full-width at half-maximum are: F435W ($4297 \pm 1038 \text{ \AA}$), F606W ($5907 \pm 2342 \text{ \AA}$), F775W ($7764 \pm 1528 \text{ \AA}$), F850L ($9445 \pm 1229 \text{ \AA}$). The limiting magnitude for point sources is $m_{\text{AB}} \sim 29$ within these images, making the UDF easily the deepest optical imaging taken to date.

The photometry and photometric redshifts we use are taken from Coe et al. (2006). Coe et al. (2006) measure the photometry of galaxies in the UDF within the UDF BVizJH bands with great care. The galaxies are detected with a modified version of SExtractor, called SEXSeg. The photometry is PSF-corrected and aperture matched, removing the problem of matching magnitudes at different wavelengths due to variations in the PSF. The z_{850} data was furthermore corrected for PSF halo effects, and a correction was made to the NICMOS photometric zero point (Coe et al. 2006). This high fidelity photometry is then used for deriving photometric redshifts, and for the stellar masses we measure for our galaxy sample.

The Coe et al. (2006) photometric redshifts are measured using the photometric redshift techniques from Benitez (2000), based on the optical and NIR photometry from ACS and NICMOS. In addition to these photometric redshifts we utilise 56 spectroscopic redshifts taken to date within the UDF field within our selection limits.

We limit our analysis of the UDF galaxies to the relatively brighter systems, although we are able to probe in the UDF down to a fainter magnitude than any other field. Faint galaxies are difficult to study structurally, as they are often too small, and have too low a surface brightness for reliable measurements. We thus limit the magnitude of our study to $z_{850} < 27$, such that we are not biased by low signal to noise imaging. We furthermore use the Coe et al. (2006) UDF image versions with their accompanying segmentation map from SExtractor, and weight map, which we utilize later in our structural analysis (§3). The final catalogue of $z_{850} < 27$ sources we study in this paper contains 1052 unique galaxies.

3 STRUCTURAL MEASURES AND STELLAR MASSES

As described in the introduction, the structures and morphologies of galaxies is quickly becoming recognised as one of the most important methods for understanding galaxies (e.g., Conselice 2003a,b; Cassata et al. 2005; Grogin et al. 2005; Trujillo et al. 2007). As such, we study the morphological properties of all $z_{850} < 27$ galaxies in the UDF in some detail. It is important however to realise what we can, and cannot, study within the UDF. Although the UDF is the deepest image ever taken, it is unfortunately not very large, with a total area of 11 arcmin^2 . This does not give a large enough co-moving volume to study galaxies in large detail at any redshift. It does allow us to probe structures and morphologies in greater detail than in any other field, although general results on galaxy evolution obtained from it are limited.

We carry out our analysis in several steps to maximise the usefulness of the data, and to minimise problems from contamination. We first create ‘postage stamp’ images of each of our sample galaxies. These are created by cutting out a $10'' \times 10''$ box of the UDF surrounding each galaxy,

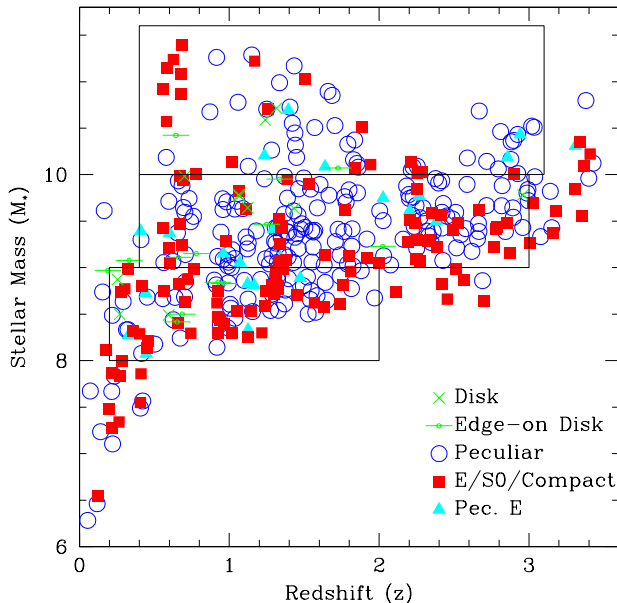


Figure 1. Stellar mass vs. redshift with the various galaxy types studied in this paper labelled. The open blue circles are the galaxies classified as peculiars, the solid red boxes are ellipticals, S0s, and compacts, while the cyan triangles are ellipticals that appear to have a peculiarity. Disk galaxies are shown as green crosses for face on systems, with the edge-on systems displayed as a dot with a solid line. The boxes on this figure denote the regions in which we measure the merger fraction later in the paper.

based on positions from the SExtractor catalog detections from Coe et al. (2006). Before this is done, the UDF ACS image is cleaned of nearby galaxies and stars through the use of the so-called ‘segmentation map’ produced by the SESSeg (§2, Coe et al. 2006). The segmentation maps are created through the SExtractor procedure used by Coe et al. (2006) for detecting galaxies within the UDF. These segmentation maps are equivalent in size to the UDF image itself, with the difference being that it gives a numerical value for each pixel that reveals which galaxy it belongs to. These segmentation maps are used for photometry, but they are also useful for removing nearby galaxies. The procedure we use is to replace pixels of galaxies not being studied to the sky background with proper noise characteristics included. We then use these cleaned cutout images in our analysis.

After examining our sample by eye, we found that occasionally features remained near galaxies, and had to be manually removed by hand. There were also cases where large late-type galaxies with spiral arms brighter than their centres tended to be picked up by the program more than once, and these were manually noted when spotted. In the following sections we describe our visual and quantitative analysis of these galaxy images within the UDF.

3.1 Visual/Classical Morphologies

We study the structures and morphologies of our sample using two broadly different methods. The first is a simple visual estimate of morphologies based on the appearance of

our galaxies in the ACS imaging. The outline of our classification process is given in Conselice et al. (2005a), and Conselice et al. (2007b). We place each UDF galaxy into one of nine categories: compact, elliptical, distorted elliptical, lenticular (S0), early-type disk, late-type disk, edge-on disk, merger/peculiar, and unknown/too-faint. Our classifications are based only on appearance. Information such as colour, size, redshift, etc are not used to determine these types. We carry out these classifications to link our results with lower redshifts, as well as for having some basis for understanding the morphological distribution of galaxies at high redshifts. A short explanation of these types is provided below, with the number we find in each class listed at the end of each description.

(i) Ellipticals : Ellipticals (Es) are centrally concentrated galaxies with no evidence for lower surface brightness, outer structures. We have 128 of these galaxies in our sample.

(ii) Peculiar-Ellipticals : Peculiar ellipticals (Pec-Es) are galaxies that appear elliptical, but have some minor morphological peculiarity, such as offset isophotes, dual nuclei, or low-surface brightness asymmetries in their outer parts (65 systems).

(iii) S0s: S0s are galaxies that appear to have a smooth disk with a bulge. These galaxies do not appear to have much star formation, and are selected in the same way nearby S0s are. Our sample has a total of three S0s, making its contribution very small.

(iv) Compact - A galaxy is classified as compact if its structure is resolved, but still appears compact without any substructure. It is similar to the elliptical classification in that a system must appear very smooth and symmetric. A compact galaxy differs from an elliptical in that it contains no obvious features such as an extended light distribution or a light envelope. (153 systems)

(v) Early-type disks: If a galaxy contains a central concentration with some evidence for lower surface brightness outer light in the form of spiral arms or a disk, it is classified as an early-type disk. (28 systems)

(vi) Late-type disks: Late-type disks are galaxies that appear to have more outer low surface brightness disk light than inner concentrated light. (5 systems)

(vii) Edge-on disks: disk systems seen edge-on, and whose face-on morphology cannot be determined, but is presumably an S0 or spiral. (32 systems)

(viii) Peculiar/irregular: Peculiars and irregulars are systems that appear to be disturbed, or peculiar looking, including elongated/tailed sources. These galaxies are possibly in some phase of a merger (Conselice et al. 2003a), or are dominated by star formation (502 systems).

(ix) Unknown/too-faint: If a galaxy is too faint for any reliable classification it was placed in this category. Often these galaxies appear as smudges without any structure. These could be disks or ellipticals, but their extreme faintness precludes a reliable classification. (77 systems)

3.2 Extended CAS Structural Analysis

We use the CAS (concentration, asymmetry, clumpiness) parameters to probe the structures of our galaxies quantitatively. The CAS parameters are a non-parametric method for measuring the forms of galaxies on resolved CCD images

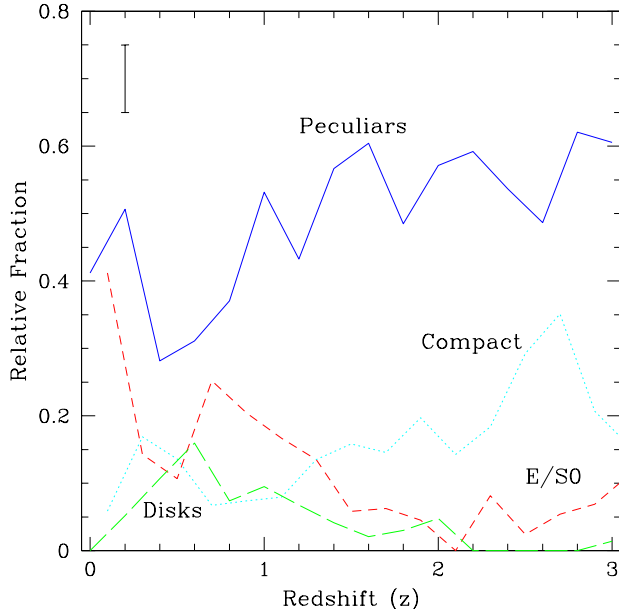


Figure 2. The relative distribution of galaxy types in the Hubble Ultra Deep Field for systems selected with $z_{850} < 27$. Labelled are disks, ellipticals/S0s, compact galaxies, and peculiars. Note that the compact galaxies become an important population at higher redshifts.

(e.g., Conselice et al. 2000a; Bershady et al. 2000; Conselice et al. 2002; Conselice 2003). The basic idea is that galaxies have light distributions that reveal their past and present formation modes (Conselice 2003). Furthermore, well-known galaxy types in the nearby universe fall in well defined regions of the CAS parameter space. For example, the selection $A > 0.35$ locates systems which are nearly all major galaxy mergers in the nearby universe (e.g., Conselice et al. 2000b; Conselice 2003; Hernandez-Toledo et al. 2005; Conselice 2006b). In addition to the classic CAS parameters, we also investigate the use of the similar Gini and M_{20} parameters (Lotz et al. 2006) for understanding the morphologies of the UDF galaxies. We give a brief description of these parameters below.

The way we measure structural parameters on the UDF image varies slightly from what has been done earlier in the Hubble Deep Field, and GOODS imaging (e.g., Conselice et al. 2003a; Conselice et al. 2004). The basic procedure, after cutting out the galaxy into a smaller image, is to first measure the radius in which the parameters are computed. The radius we use for all our indices is the Petrosian radii, which is the radius defined as the location where the surface brightness at a given radius is 20% of the surface brightness within that radius (e.g., Bershady et al. 2000; Conselice 2003). We use circular apertures for our Petrosian radii and quantitative parameter estimation. We begin our estimates of the galaxy centre for the radius measurement at the centroid of the galaxy’s light distribution. Through modelling and various tests, it can be shown that the resulting radii do not depend critically on the exact centre, although the CAS

and other parameters do (Conselice et al. 2000; Lotz et al. 2004). The exact Petrosian radius we use to measure our parameters is

$$R_{\text{Petr}} = 1.5 \times r(\eta = 0.2),$$

where $r(\eta = 0.2)$ is the radius where the surface brightness is 20% of the surface brightness within that radius.

A very important issue, especially for the faint galaxies seen in the UDF, is how to account for background light and noise. For faint galaxies there is a considerable amount of noise added due to the sky, which must be corrected. Through various test, outlined in detail in Conselice et al. (2008, in prep), we conclude that the proper way to correct parameters for the background requires that the selected background area be close to the object of interest. This is only an issue for faint galaxies, and for galaxies imaged on large mosaics which have a non-uniform weight map, and whose noise characteristics vary across the field. By using a background near each object we alleviate these issues as the noise properties do not vary significantly over $\sim 0.5 - 1$ arcmin, where the galaxy and the background area are selected. We review below how the CAS and Gini/ M_{20} parameters are measured. For more detail see Bershady et al. (2000), Conselice et al. (2000), Conselice (2003) and Lotz et al. (2006).

3.2.1 Asymmetry

The asymmetry of a galaxy is measured by taking an original galaxy image and rotating it 180 degrees about the galaxy centre, and then subtracting the two images (Conselice 1997). There are corrections done for background, and radius (explained in detail in Conselice et al. 2000a). Most importantly, the centre for rotation is decided by an iterative process which finds the location of the minimum asymmetry. The formula for calculating the asymmetry is given by:

$$A = \min \left(\frac{|\Sigma|I_0 - I_{180}|}{\Sigma|I_0|} \right) - \min \left(\frac{|\Sigma|B_0 - B_{180}|}{\Sigma|I_0|} \right) \quad (1)$$

Where I_0 is the original image pixels, I_{180} is the image after rotating by 180° . The background subtraction using light from a blank sky area, called B_0 , are critical for this process, and must be minimised in the same way as the original galaxy itself. A lower value of A means that a galaxy has a higher degree of rotational symmetry which tends to be found in elliptical galaxies. Higher values of A indicate an asymmetric light distribution, which are usually found in spiral galaxies, or in the more extreme case, merger candidates. The upper and lower bound for A , in this study are 1.18 and ~ 0 . The mean A value is 0.26.

3.2.2 Concentration

Concentration is a measure of the intensity of light contained within a central region in comparison to a larger region in the outer-parts of a galaxy. The exact definition is the ratio of two circular radii which contain 20% and 80% (r_{20} , r_{80}) of the total galaxy flux,

$$C = 5 \times \log \left(\frac{r_{80}}{r_{20}} \right). \quad (2)$$

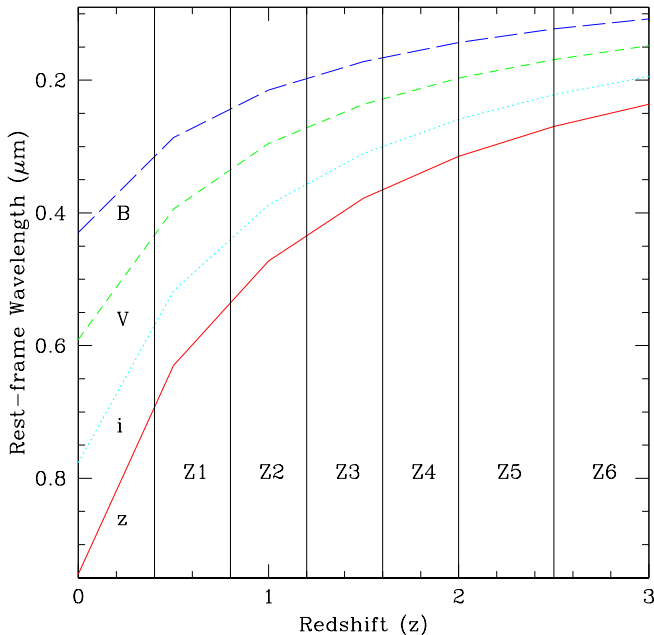


Figure 3. The rest-frame wavelength probed as a function of redshift for each of our filters used in this study - B_{450} , V_{606} , i_{775} and z_{850} . The vertical line denote the redshift ranges we use to divide our sample into various redshift cuts.

This index is sometimes called C_{28} . A higher value of C indicates that a larger amount of light in a galaxy is contained within a central region. The upper and lower bounds of C for our galaxy sample are $C = 1.8 - 4.4$, with a mean of $C = 2.77$. This particular measurement of the concentration correlates well with the mass and halo properties of galaxies (e.g., Bershady et al. 2000; Conselice 2003; Courteau et al. 2007).

3.2.3 Clumpiness

The clumpiness (sometimes called smoothness) S is a parameter used to describe the fraction of light in a galaxy which is contained in clumpy light concentrations. Clumpy galaxies have a relatively large amount of light at high spatial frequencies, whereas smooth systems, such as elliptical galaxies contain light at low spatial frequencies. Galaxies which are undergoing star formation tend to have very clumpy structures, and high S values. Clumpiness can be measured in a number of ways, the most common method used, as described in Conselice (2003) is,

$$S = 10 \times \left[\left(\frac{\Sigma(I_{x,y} - I_{x,y}^\sigma)}{\Sigma I_{x,y}} \right) - \left(\frac{\Sigma(B_{x,y} - B_{x,y}^\sigma)}{\Sigma I_{x,y}} \right) \right], \quad (3)$$

where, the original image $I_{x,y}$ is blurred to produce a secondary image, $I_{x,y}^\sigma$. This blurred image is then subtracted from the original image leaving a residual map, containing only high frequency structures in the galaxy (Conselice 2003). To quantify this, we normalise the summation of these

residuals by the original galaxy’s total light, and subtract from this the residual amount of sky after smoothing and subtracting it in the same way. The size of the smoothing kernel σ is determined by the radius of the galaxy, and is $\sigma = 0.2 \cdot 1.5 \times r (\eta = 0.2)$ (Conselice 2003). Note that the centres of galaxies are removed when this procedure is carried out.

3.2.4 Gini Coefficient

The Gini coefficient is a statistical tool originally used in economics to determine the distribution of wealth within a population, with higher values indicating a very unequal distribution (Gini of 1 would mean all wealth/light is in one person/pixel), while a lower value indicates it is distributed more evenly amongst the population (Gini of 0 would mean everyone/every pixel has an equal share). The value of G is defined by the Lorentz curve of the galaxy’s light distribution, which does not take into consideration spatial position. Each pixel is ordered by its brightness and counted as part of the cumulative distribution (see Lotz et al. 2004, 2006). The mean value of Gini in our UDF catalogue is 0.71.

3.2.5 M_{20}

The M_{20} parameter is a similar parameter to the concentration in that it gives a value that indicates whether light is concentrated within an image; it is however calculated slightly differently. The total moment of light is calculated by summing the flux of each pixel multiplied by the square of its distance from the centre. The centre is deemed to be the location where M_{20} is minimised (Lotz et al 2004). The value of M_{20} is the moment of the fluxes of the brightest 20% of light in a galaxy, which is then normalised by the total light moment for all pixels (Lotz et al. 2004, 2006)

The main differences between M_{20} and C are due to the moments in M_{20} which depend on the distance from the galaxy centre. The value of M_{20} will therefore be more affected by spatial variations, and also the centre of the galaxy is again a free parameter. This can make it more sensitive to possible mergers. In our study we find that the upper and lower bounds of M_{20} are $M_{20} = 0$ to $M_{20} = -2.51$, with a mean of $M_{20} = -1.45$.

3.3 Overview of Measured CAS/G/ M_{20} Values

We apply a revised CAS system to our UDF galaxy sample to determine their structural parameters. There are several caveats to using the ACS imaging to measure these parameters. The first is that there are morphological k -correction and surface brightness dimming effects which will change

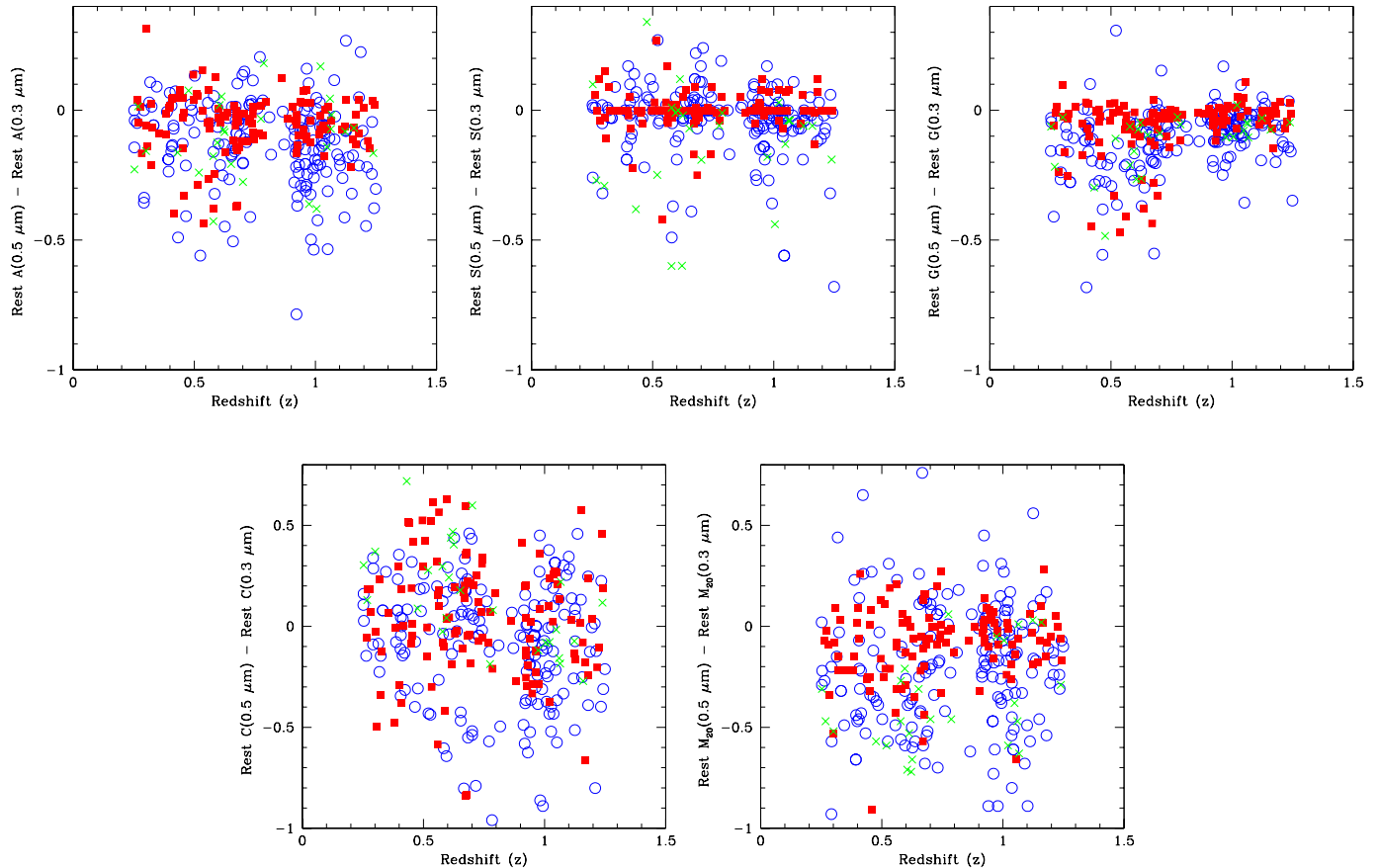


Figure 4. The change in the CAS and Gini and M_{20} parameters as a function of redshift. We trace in this figure the change between the rest-frame $0.5 \mu\text{m}$ and $0.3 \mu\text{m}$ morphology. The concentration and M_{20} values have a much larger dynamical range than the CAS and Gini values which is intrinsic to the way these are measured (see text). In relative terms these changes are similar within the other parameters. The symbols are the same as in Figure 1.

the measured parameters, such that the asymmetry and clumpiness indices will decrease (Conselice et al. 2000a; Conselice 2003), and the concentration index will be less reliable (Conselice 2003). There is also the issue that for systems at $z > 1.2$ we are viewing these galaxies in their rest-frame ultraviolet using ACS data, which means that there are complications when comparing their measured structures with the calibrated rest-frame optical indices for nearby galaxies. We deal with the first problem in §4.2 and discuss the reliability of the measurements themselves below.

To test the reliability of our parameters, we plot all five indices against apparent magnitude to our $z_{850} = 27$ magnitude limit. We find that there is no dependence on magnitude for the morphological parameters within this limit. At magnitudes fainter than our limit we find that all of our structural parameters become systematically smaller or higher, simply just due to a lower signal to noise. Our limit of $z_{850} < 27$ ensures that we are within the regime where systematic problems are not dominating our signal.

3.4 Stellar Masses

The stellar masses we measure are computed using the techniques described in Bundy et al. (2006) and Conselice et al. (2007b) using the $BVizJH$ data. The basic method we use consists of fitting a grid of model SEDs constructed from Bruzual & Charlot (2003) (BC03) stellar population synthesis models, with different star formation histories. We use an exponentially declining model to characterise the star formation, with various ages, metallicities and dust contents included. These models are parameterised by an age, and an e-folding time for parameterising the history of star formation. These parameterisations are fairly simple, and it remains possible that stellar mass from older stars is missed under brighter younger populations. However, stellar masses measured through our technique are roughly the expected factor of 5-10 smaller than dynamical masses at $z \sim 1$ using a sample of disk galaxies (Conselice et al. 2005b), demonstrating their inherent reliability. We furthermore test how these stellar masses would change utilising the newer Bruzual & Charlot (2007) models, finding at most a 0.07 dex decrease

Table 1. The change in CAS and Gini/ M_{20} parameters from the rest-frame optical to near-UV as function of redshift. These values are defined such that $\Delta = \lambda(0.5\mu m) - \lambda(0.3\mu m)$

Peculiars	$z = 0.25 - 0.75$	$z = 0.75 - 1.25$
$\frac{\Delta C}{\Delta \lambda} (\mu m^{-1})$	-0.09 ± 1.50	-0.78 ± 2.30
$\frac{\Delta A}{\Delta \lambda} (\mu m^{-1})$	-0.26 ± 0.91	-0.83 ± 1.06
$\frac{\Delta S}{\Delta \lambda} (\mu m^{-1})$	-0.48 ± 0.57	-0.33 ± 0.61
$\frac{\Delta G}{\Delta \lambda} (\mu m^{-1})$	-0.65 ± 0.65	-0.39 ± 1.22
$\frac{\Delta M_{20}}{\Delta \lambda} (\mu m^{-1})$	-0.91 ± 1.50	-1.00 ± 1.94
Ellipticals	$z = 0.25 - 0.75$	$z = 0.75 - 1.25$
$\frac{\Delta C}{\Delta \lambda} (\mu m^{-1})$	0.43 ± 1.50	-0.11 ± 1.50
$\frac{\Delta A}{\Delta \lambda} (\mu m^{-1})$	-0.26 ± 0.61	-0.22 ± 0.56
$\frac{\Delta S}{\Delta \lambda} (\mu m^{-1})$	-0.04 ± 0.43	0.06 ± 0.33
$\frac{\Delta G}{\Delta \lambda} (\mu m^{-1})$	-0.43 ± 0.78	-0.11 ± 0.61
$\frac{\Delta M_{20}}{\Delta \lambda} (\mu m^{-1})$	-0.69 ± 1.26	-0.21 ± 0.69
Spirals	$z = 0.25 - 0.75$	$z = 0.75 - 1.25$
$\frac{\Delta C}{\Delta \lambda} (\mu m^{-1})$	1.30 ± 0.87	-0.33 ± 2.30
$\frac{\Delta A}{\Delta \lambda} (\mu m^{-1})$	-0.57 ± 0.57	-0.44 ± 1.40
$\frac{\Delta S}{\Delta \lambda} (\mu m^{-1})$	-0.61 ± 1.13	-0.56 ± 1.20
$\frac{\Delta G}{\Delta \lambda} (\mu m^{-1})$	-0.70 ± 0.57	-0.33 ± 0.83
$\frac{\Delta M_{20}}{\Delta \lambda} (\mu m^{-1})$	-2.30 ± 1.00	-1.04 ± 1.70

due to the newer implementation of thermal-pulsating AGB stars (see also Conselice et al. 2007b).

We calculate the likely stellar mass, age, and absolute magnitudes for each galaxy at all star formation histories, and determine stellar masses based on this distribution. Distributions with larger ranges of stellar masses have larger resulting uncertainties. It turns out that while parameters such as the age, e-folding time, metallicity, etc. are not likely accurately measured in these calculations, due to various degeneracies, the stellar mass is robust. Typical errors for our stellar masses are 0.2 dex from the width of the probability distributions. There are also uncertainties from the choice of the IMF. Our stellar masses utilise the Salpeter IMF, which can be converted to Chabrier IMF stellar masses by subtracting 0.25 dex. There are additional random uncertainties due to photometric errors. The resulting stellar masses thus have a total random error of 0.2-0.3 dex, roughly a factor of two. This fitting method gives similar results used to compute merger fractions as a function of stellar mass in previous work (Conselice et al. 2003a).

4 RESULTS

4.1 General Features

By plotting our visual estimates of morphology vs. various properties, we can decipher the formation modes of galaxies found at a faint z_{850} magnitude limit. Figure 1 plots stellar mass versus redshift for our sample, with the various morphological types labelled. All galaxy types are seen at all redshifts, and at nearly all masses. As can also be seen, there is a slight increase in the upper envelope of stellar masses at $z < 1$. While we find galaxies with masses $M_* > 10^{10} M_\odot$ at all redshifts, in general there are few galaxies with masses $M_* > 10^{11} M_\odot$ at any redshift, demonstrating

how difficult it is to study these systems within small fields like the UDF and HDFs (Conselice et al. 2007b).

We also plot the fraction of types at our z_{850} limit as a function of redshift in Figure 2. Figure 2 shows that galaxies that look peculiar by eye dominate the galaxy population at all redshifts within a $z_{850} = 27$ magnitude selection limit. This is especially true at higher redshifts, where galaxies that look unusual make up roughly half of the galaxy population. This appears to be a different morphological distribution with redshift than what has been seen in the past using absolute magnitudes and stellar masses (e.g., Conselice et al. 2005a). We can explain this difference through our use of an apparent magnitude limit, rather than an absolute magnitude limit. It has been known since the first deep HST imaging (e.g., Driver et al. 1998; Glazebrook et al. 1995) that at fainter magnitudes there are more peculiar galaxies. There are also more fainter galaxies than brighter ones, thus it is not surprising that peculiars are the dominant population (e.g., Elmegreen et al. 2005; Ravindranath et al. 2006). If we do a stellar mass cut at a high limit, such as $M_* > 10^{9.5} M_\odot$, we find that the peculiars no longer dominate the population.

The other reason for the apparently large number of peculiars is that the higher resolution of the ACS camera makes it easy to detect peculiar features that otherwise would not be identifiable within WFPC2 imaging. This is particularly true for galaxies that would be considered spirals or disks, but lack a coherent obvious structure in their morphological appearance as seen within ACS.

It is also worth noting a few more interesting features of Figure 2. The first is that while the peculiars dominate the galaxy population within the $z_{850} < 27$ selection, the ellipticals and disks decline in their relative contributions at lower redshifts. However, at redshifts > 1.5 the galaxies classified by eye as compacts are an important part of the galaxy population, with a fraction of 20-35%. This is a significant fraction of the galaxy population, particularly at $z > 2$ and it is worth briefly describing what these systems are. From Figure 1 we can see that these galaxies have high stellar masses with $M_* > 10^9 M_\odot$, and often $M_* > 10^{10} M_\odot$. These systems could be the progenitors of ellipticals seen at lower-redshifts, or could be a separate galaxy population that is in some form of evolution.

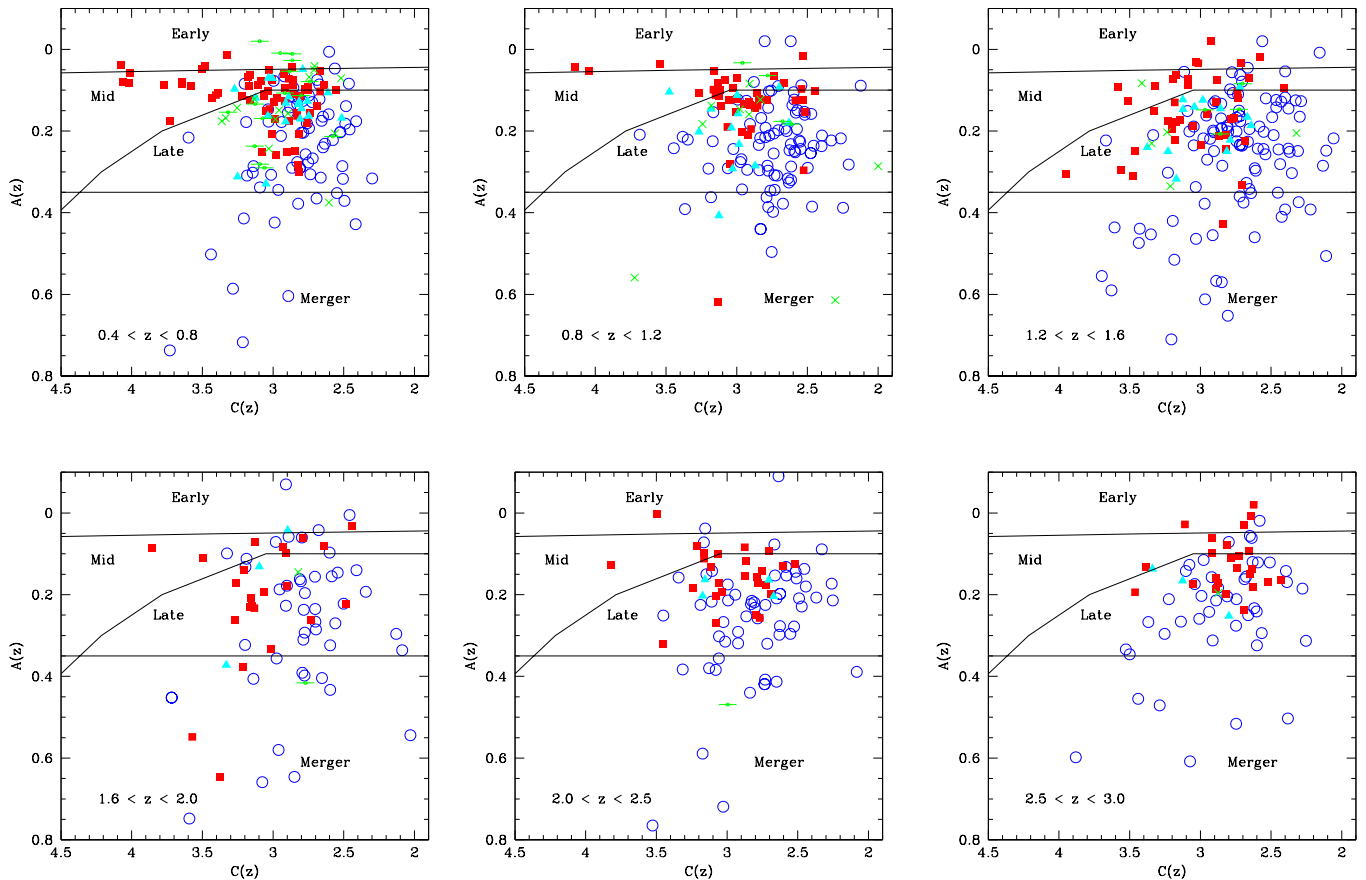


Figure 5. The distribution of our galaxy sample in the UDF as seen in the concentration-asymmetry plane. The lines on each plot denote the region in which different galaxy types, as seen in the rest-frame optical are found in the nearby universe (e.g., Bershady et al. 2000; Conselice 2003). The redshift range for each panel follows the division seen in Figure 3, and is labelled at the bottom of each panel. The symbol types for the points are the same as in Figure 1.

4.2 The Morphological K-Correction

One of the major problems with studying galaxy structure and morphology is that these features can depend quite strongly on the rest-frame wavelength probed (e.g., Hibbard & Vacca 1997; Windhorst et al. 2002; Papovich et al. 2003; Taylor-Mager et al. 2007). To understand this issue within the UDF, we determine how our quantitative indices change as a function of wavelength at $z < 1$, where we probe light from the rest-frame ultraviolet to the rest-frame B-band for the same galaxies, using our four ACS filters.

For various reasons it is important to determine how galaxy structure changes as a function of wavelength, and the UDF, due to its depth, is the ideal place to carry this out by directly probing these differences. We can furthermore use these results later when we do not have a full set of ACS-UDF filters, or as often happens, we do not have a filter which probes the rest-frame optical at higher redshifts. Until the advent of a high resolution near-infrared camera, such as WFC3 on Hubble, ACS optical imaging is our only probe of high resolution imaging at $z > 1.2$.

We calculate morphological K-corrections in a number

of ways. The first way is to simply determine how the CAS, Gini, and M_{20} parameters change as a function of wavelength and redshift. We define a quantify, ΔP_λ , which is the change in the quantitative parameter values per unit wavelength (μm). The values of ΔP_λ change as a function of rest-frame wavelength (λ), redshift (z), quantitative parameter (CAS, G, M_{20}), and the eye-ball estimates of the morphological type (T). We quantify the morphological K-correction by,

$$\Delta P_\lambda(\lambda, z, T) = \frac{\delta P(\lambda_1 - \lambda_2)}{\delta \lambda}, \quad (4)$$

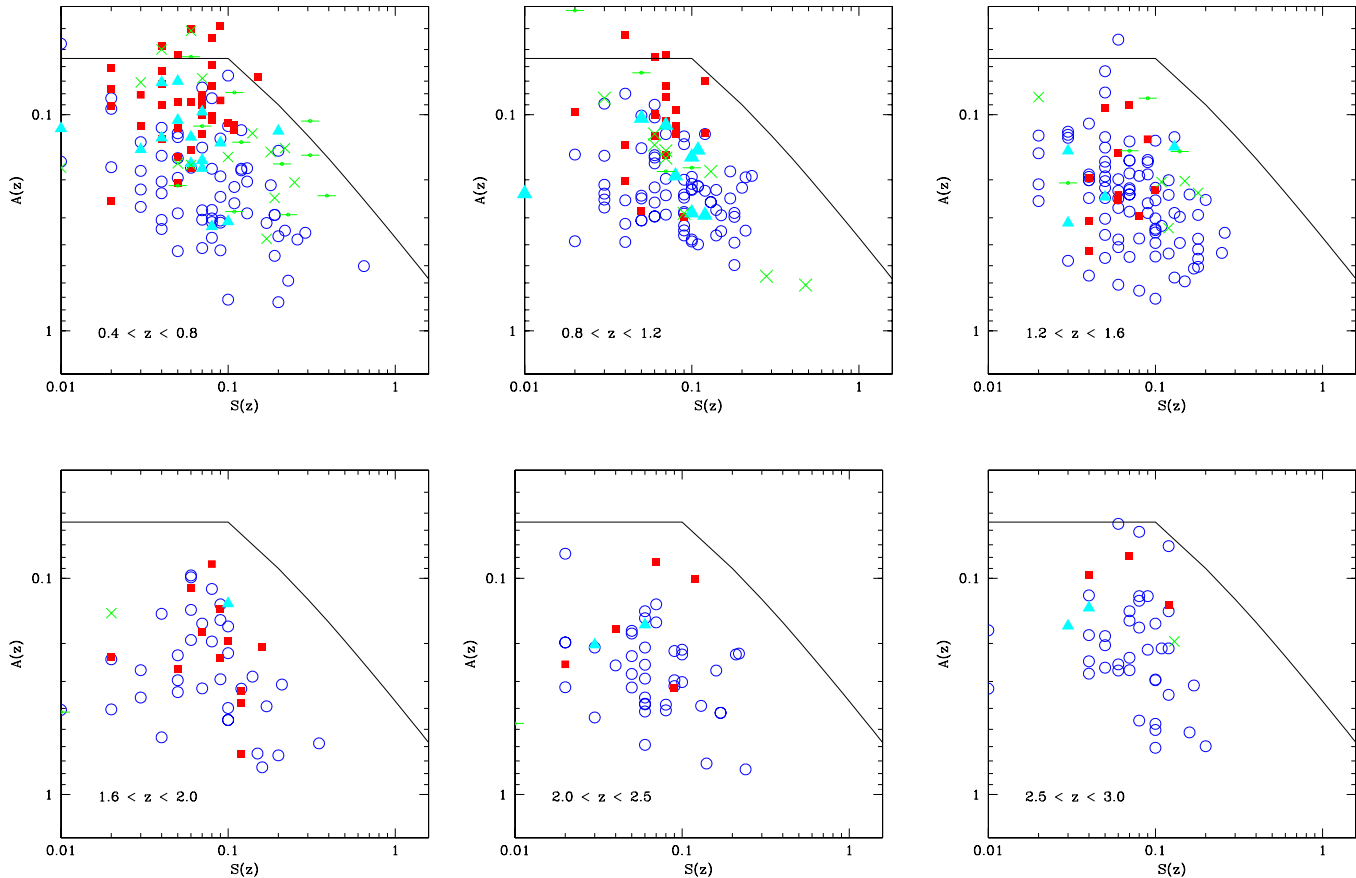


Figure 6. The relation between the asymmetry (A) and clumpiness (S) for our sample of UDF galaxies in the observed z_{850} band. The solid line shows the relationship between these two parameters as found for nearby galaxies that are not involved in mergers (Conselice 2003). This relationship is such that non-merging galaxies with a higher clumpiness has a slightly higher asymmetry, both due to star formation. Merging galaxies, where the structure is distorted due to bulk asymmetries from a merger have a larger asymmetry for their clumpiness. The point symbols are the same as in Figure 1 and the redshift range for each individual panel is listed.

where δP is the change in the parameter of interest between λ_1 and λ_2 , and $\delta\lambda$ is the change in rest-frame wavelength measure in microns. Before describing how ΔP_λ varies with redshift and quantitative parameter, it is important to re-motivate why we are interested in this quantity.

The highest redshifts we probe in this paper are $z \sim 2.5 - 3$. When we observe galaxies at these redshifts in our reddest observed band (z_{850}), we are viewing them in the rest-frame ultraviolet at $\sim 2700 \text{ \AA}$ (see Figure 3). Due to our suite of four ACS filters, this same rest-frame wavelength is probed by the observed B_{450} -band for galaxies at $z \sim 0.5$,

the V_{606} -band for galaxies at $z \sim 1$, and the i_{775} -band for galaxies at $z \sim 2$ (Figure 3). We can therefore determine at lower redshifts how quantitative indices may change between the rest-frame optical and rest-frame ultraviolet at higher redshifts as a function of apparent morphological type (see Conselice et al. 2005a for a direct measurement of this using NICMOS imaging in the Hubble Deep Field).

Figure 4 and Table 1 show the results of this investigation. We plot and list the differences between the values of our parameters in the rest-frame $0.3 \mu\text{m}$, and at rest-frame $0.5 \mu\text{m}$ (Figure 4). We limit this analysis to those galaxies which are at $z < 1.25$, as at higher redshifts we are no longer probing above the 4000 \AA break (Figure 3). For this analysis we take the values in the observed z_{850} and V_{606} bands for galaxies between $z = 0.75 - 1.25$, and i_{775} and B_{435} for galaxies between $z = 0.25 - 0.75$. This lets us probe the quantitative structural k -correction between the rest-frame near-ultraviolet at $< 300 \text{ nm}$, and the rest-frame B-band at $\lambda \sim 500 \text{ nm}$.

We find that the change in galaxy quantitative parameters between the rest-frame UV and the rest-frame optical, ΔP_λ , varies amongst morphological type, as well as redshift.

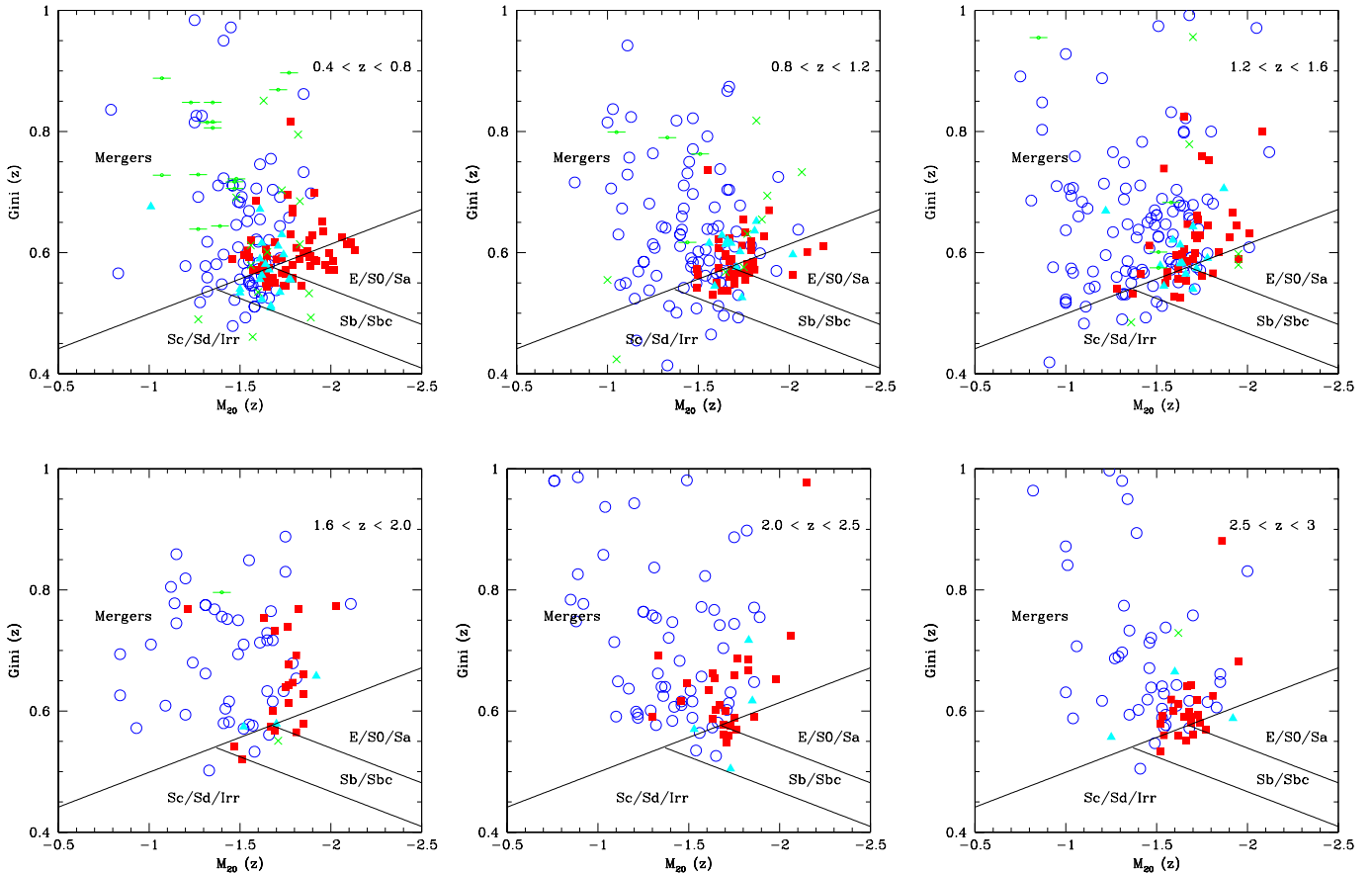


Figure 7. The relationship between the Gini and M_{20} index in the observed z_{850} band for our sample of UDF galaxies. The lines and symbols denote the region where different nearby galaxy types are found (Lotz et al. 2006). The redshift range for each individual panel are the same as in Figure 5 & 6. The symbols for the points are the same as in Figure 1

As Figure 4 shows, the galaxy type with the most variation between optical and near-UV are the peculiars. For the asymmetry and clumpiness indices we find that the value of ΔP_λ is largest for the peculiar galaxies at higher redshifts, compared with other morphological types. We do not find such a large differential between galaxy types within the other parameters. This reveals that this difference between the A and S parameters for the peculiars is likely driven at least partially by star formation present within these systems.

Note that the concentration and M_{20} values have a larger dynamical range than the A , S and Gini parameters, which accounts for the larger differences seen (Figure 4). However, when we normalise these differences by their initial values we find that the range is relatively similar to the other parameters, particularly for the concentration index, whose values only change by $\delta C/C = -0.1$ on average.

As Table 1 shows, most of the calculated values of ΔP_λ are similar at $z = 0.25 - 0.75$ as at $z = 0.75 - 1.25$. The exceptions to this are the concentration, M_{20} and Gini indices for the spirals, and the concentration index for both the peculiars and ellipticals, and the asymmetries for the

peculiars. Perhaps surprisingly, the most stable parameter is the S index, which has the smallest value of ΔP_λ of all the parameters. This is likely due to the fact that the high resolution and high depth of the ACS images allows us to reveal the fine structure in these galaxies at all observed wavelengths.

The likely reason for these changes, at least in terms of the concentration index, is that the star formation rate for these galaxies, and all galaxies at $z < 1$, is declining. This results in the differences between a blue and a UV band becoming even more pronounced, as there is not as much star formation to create a large signal in the ultraviolet. This is the reason the ellipticals change in concentration from a negative gradient to a relatively large positive one. Since star formation is seen in ellipticals at $z \sim 1$ (e.g., Stanford et al. 2004; Teplitz et al. 2006), we are likely witnessing a lack of star formation at the lower redshifts. We utilise these results in the later discussion of this paper on the merger fraction for these galaxies, and how to interpret structural indices at higher redshifts.

4.3 Quantitative Structure

There are a few very popular method for ‘classifying’ galaxies via quantitative parameters. These are the concentration-asymmetry plane (e.g., Bershady et al. 2000), the asymmetry-clumpiness plane (Conselice 2003), and the Gini/ M_{20} plane (Lotz et al. 2004, 2006). We investigate where eye-ball estimates of galaxy types fall into these different areas of quantitative structural space at $0.4 < z < 3$, as well as how the various values agree, or otherwise, with each other.

4.3.1 The Concentration-Asymmetry plane

Figure 5 shows the UDF concentration-asymmetry plane, without redshift corrections applied (Conselice 2003), as observed in the z_{850} -band. The lines on this diagram denote the general area where early/mid/late and merging galaxies are located in this space (Bershady et al. 2000; Conselice 2003). One of the most striking aspects of Figure 5 is that very few galaxies appear in the early region; this is due to a higher general level of asymmetry within UDF galaxies in comparison to the local universe. Interestingly, this is true of the galaxies classified as early types, a very small percentage of which actually fall within the early region at any redshift.

The disk galaxies, as classified by eye, appear in the late area of the plot where they are expected to be found, although there are a few that appear above the merger limit of $A = 0.35$. These disk galaxies are always very clumpy systems which appear to have multiple components. The edge-on galaxies are however distributed quite randomly around the plot, but they generally contain a low asymmetry. Most are located in the late-type region on the CA space.

Another interesting trend is that the disturbed ellipticals (the cyan triangles in Figure 5) fall in a buffer zone between early-types and the peculiar galaxies. Most of them are in fact within the late-type region, although these galaxies do not have a disk morphology. This suggests that these galaxies are within an intermediate state of formation between the peculiar galaxies and the relaxed ellipticals. Figure 5 also shows how the concentration-asymmetry plane varies with redshift. The concentrated early-types do not appear to exist at higher redshifts. While at $0.4 < z < 0.8$ there are many early-types with a high light concentration, very few of these systems are found at higher redshift. This is likely an effect of their formation, which can also be seen in the growth of stellar masses for early-types, where few very massive systems are found at $z > 1$ (Figure 1).

As Figure 5 shows, the asymmetry index is very good at finding galaxies which are classified by eye as peculiar/merger. There are only a few cases where galaxies which were classified as something other than a peculiar are found in the region where mergers are expected, $A > 0.35$. In summary at $0.4 < z < 3$ we find that $86 \pm 10\%$ of galaxies which are at $A > 0.35$ are classified as peculiars. This method also finds $20 \pm 3\%$ of the galaxies classified as peculiars are within the $A > 0.35$ region, with 82 of the classified peculiars out of 410 in the $A > 0.35$ regime. These relative fractions do not change significantly at different redshifts up to $z \sim 3$.

When we go to higher redshifts a few interesting patterns are seen. The first is that the classified ellipticals, on average, have a higher asymmetry, and lower concentration.

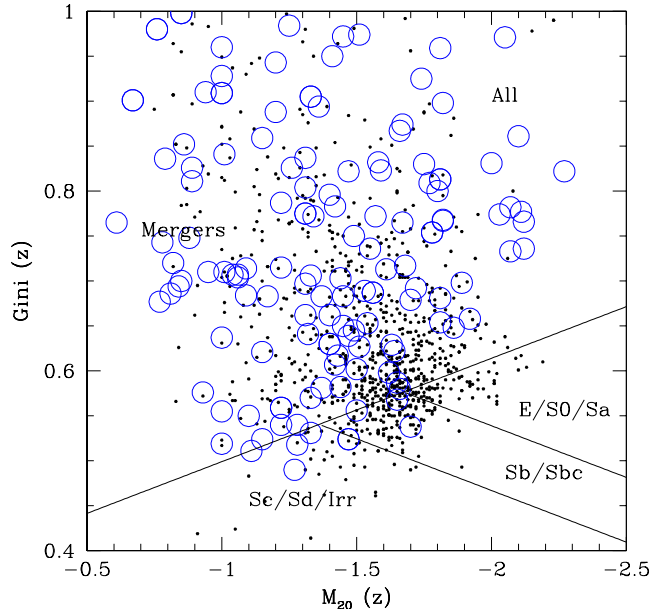


Figure 8. The Gini vs. M_{20} diagram for our entire UDF sample at all redshifts in the observed z_{850} band. The solid blue circles show the location of galaxies which are identified through the CAS method as a major merger, $A > 0.35$. The small points show those objects which have an asymmetry value of $A < 0.35$. As can be seen, in general the galaxies identifiable as a merger within the CAS system would also be identified as merger within the Gini- M_{20} plane. However, there are objects within the merger region which would not be identified as a merger within CAS.

Within $0.4 < z < 0.8$ the average values are $\langle A \rangle = 0.13$ and $\langle C \rangle = 3.1$. Up to $z \sim 1.6$ these values remain roughly the same. However at $1.6 < z < 2$ these values change to $\langle A \rangle = 0.21$ and $\langle C \rangle = 3.1$. While the average concentration remains the same, the average asymmetry is much higher. As we are probing the near-UV with this filter at these redshifts, this likely shows that these systems are becoming more dominated by star formation at this epoch.

In general, we find a very similar pattern within the CA space where the peculiars and early-types are found. While we cannot know from this study whether these early-types are in fact the progenitors of the early-types we see today, none the less the fact that the visually classified early-types are systematically less asymmetric than the peculiars, out to $z \sim 3$, shows that the method of classification within the CA space generally provides a good separation between galaxy types as identified by eye.

4.3.2 Clumpiness-Asymmetry Plane

Figure 6 shows the relation between clumpiness (S) and asymmetry (A) for our sample of galaxies within the UDF. The solid line shown is the $z = 0$ relation between S and A for non-merging nearby galaxies (Conselice 2003). Generally, galaxies which fall along or near this line have a structure which is dominated by star formation, which produces high clumpiness values, as well as a higher asymmetry. As can be seen in Figure 6, few of our galaxies appear to follow this

line, and most are more asymmetric at a given clumpiness than what is expected based on the $z = 0$ relation.

There are two reasons why these galaxies appear to deviate from the $z \sim 0$ relation between A and S . The first is simply due to resolution and S/N effects which will lower the level of asymmetry and clumpiness. Both the asymmetry and the clumpiness will decline when galaxies are simulated at higher redshifts, however, the clumpiness values are affected to a larger degree than the asymmetry (Conselice 2003). Simulations show that in general the typical difference is $A - S \sim 0.2$. Shifting galaxies by 0.2 dex in S however does not account for the fact that so many galaxies do not fall near the $z \sim 0$ relationship between these two quantities.

By examining the $0.4 < z < 0.8$ redshift range, we can get some idea for which types of galaxies deviate most from the non-merging galaxy relation, and perhaps understand why. First, as can be seen in Figure 6, most of the high- S galaxies at $S > 0.1$ are either disk galaxies, or peculiars, while most of the high- A systems are peculiars. When we apply the $A - S = 0.2$ redshift correction most of the disk galaxies fall near, or within, the region of the $z \sim 0$ relation. Not surprisingly, the galaxies which do not fall near this relation are the peculiars, the peculiar ellipticals, and in some cases the ellipticals themselves. These trends generally remain, although the peculiars and the ellipticals occupy a very similar part of parameter space at higher redshifts, which is not the case for the $A - C$ plane where these types can be distinguished (§4.3.1).

4.3.3 The Gini- M_{20} plane

In addition to the CAS values, the newer Gini and the M_{20} coefficients also give information on morphological characteristics of galaxies (e.g., Abraham et al. 2003; Lotz et al. 2004; Lotz et al. 2006). We show in Figure 7 the relation between Gini and M_{20} for galaxies within the UDF up to $z \sim 3$. Areas to the right of this figure (in the low M_{20} regime) are where galaxies which are more centrally concentrated in light are found. For example, early-type galaxies appear on the right side of this space, as these galaxies have a very central light concentration.

Similarly, galaxies with larger Gini indices indicate systems where a large majority of the light is contained in few pixels. While lower Gini values indicate galaxy images that have light profiles spread more evenly amongst all the pixels. Using this framework, Lotz et al. (2006) determined that various cuts in the Gini- M_{20} space can be used to separate galaxies of various types. We plot these lines and the galaxy types they denote on Figure 7.

The Gini- M_{20} plane does a fairly good job of separating galaxy types as identified by eye. This is particularly so when examining galaxies in the rest-frame optical at $z < 1.4$ (Figure 7). As can be seen within the redshift range $0.4 < z < 0.8$, the peculiars generally have a higher Gini index and are mostly found within the merger region specified by Lotz et al. (2006). However, as shown in Figure 7 there are many galaxies classified as a peculiar which are within the non-merger region, specifically in the Sc/Sd/Irr and Sb/Sbc regime. There are also many galaxies classified as early-type and especially edge-on disk, which are within the merger region.

Within the $0.4 < z < 0.8$ redshift range 75±10% of the galaxies classified by eye as peculiars are within the Gini/ M_{20} merger defined region. However, only 44±6% of the galaxies within the merger regime at these redshifts are classified as peculiars. Most other galaxy types are within this region, including nearly all of the edge-on disks, ellipticals, and face-on disks themselves. As can be seen in Figure 7, the ellipticals/S0s/compacts are the only galaxies found within the E/S0/Sa region of Gini- M_{20} space.

At higher redshift, this remains the same up to $z \sim 2$. At $0.8 < z < 1.2$ we find that 78±10% of the peculiars are in the mergers region, and 63±8% of galaxies within the mergers region are classified as peculiars. The equivalent quantities at higher redshifts are (fraction peculiar detected, fraction peculiar in region): $1.2 < z < 1.6$: (84±9%, 66±7%); $1.6 < z < 2.0$: (93±14%, 66±10%); $2.0 < z < 2.5$: (97±13%, 71±9%); $2.5 < z < 3.0$: (93±15%, 67±10%). Generally, the Gini- M_{20} method identifies a higher fraction of the peculiar galaxies as mergers, yet it has a higher contamination of non-peculiar galaxies within the merger region. As has been known from several investigations, it is necessary to clean a Gini/ M_{20} catalog of merger candidates before using it to determine the merger fraction (Lotz et al. 2006), which is generally also the case for the CAS method (De Propriis et al. 2007).

What we find at higher redshifts is a similar pattern as at the $0.4 < z < 0.8$ redshift range, although the early-types tend to drift into the higher Gini and higher M_{20} regime, revealing that these galaxies are becoming less concentrated with time in the observed z_{850} -band, as seen in the CAS parameters (§4.3.1). At the highest redshifts we find that very few of the galaxies classified by eye as an early-type are within this region, and in some cases these early-type classified galaxies are scattered throughout the merger selection. However, it is generally the case that the galaxies picked out by eye as peculiars are within the merger region and have more extreme Gini and M_{20} values than the early-types or disk galaxies.

4.4 Merger Comparisons

In this section we examine how the various methods used to define merging galaxies compare with each other. We limit this discussion to the merging galaxies, as identifying other galaxy types, such as ellipticals and especially different types of disk galaxies is more difficult and will likely require additional indices (e.g., Conselice 2003).

There have been various propositions for how to identify mergers within the CAS and Gini/ M_{20} space. As described in Conselice (2003) one method for finding mergers is to use the conditions,

$$A > 0.35 \ \& \ A > S, \quad (5)$$

where this criteria is basically that the asymmetry must be higher than an absolute limit of 0.35, which is the limit in which local mergers are found (Conselice et al. 2000a,b; Conselice 2003), and the relative definition of $A > S$ ensures that the asymmetric light is not dominated by clumpy star-forming regions.

Equation (5) is a strong restriction, and will likely miss many galaxies that are within some phase of a merger, as is already known from examining a large sample of nearby

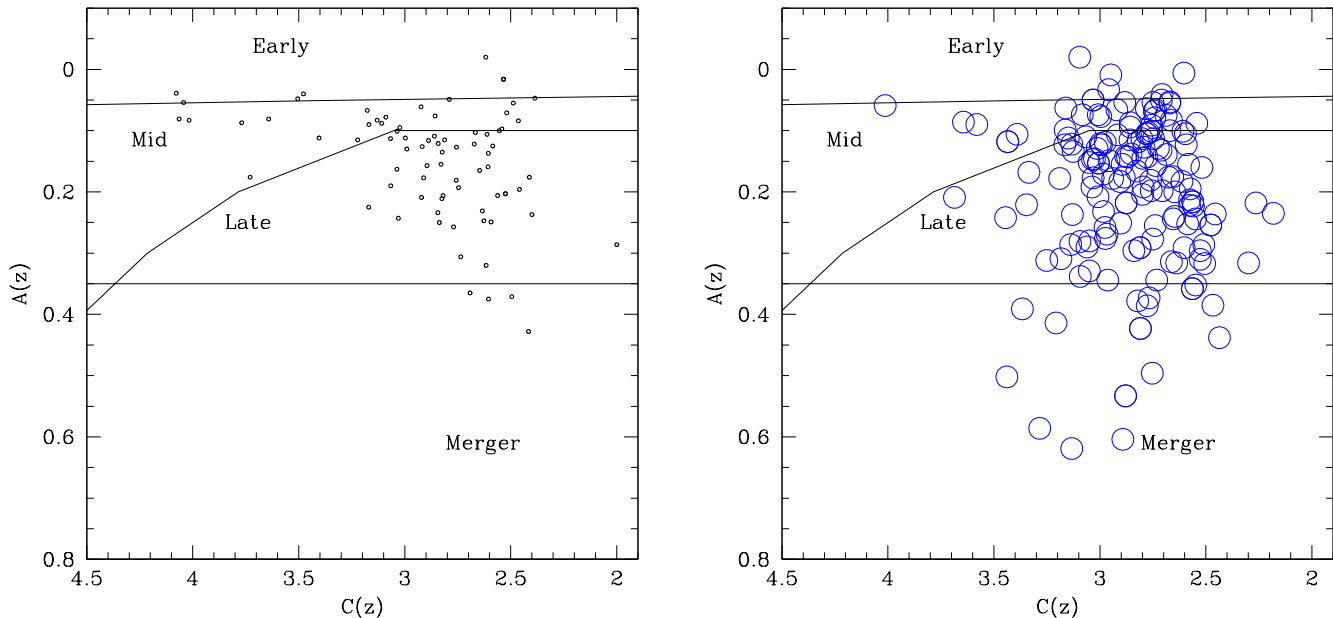


Figure 9. The concentration-asymmetry plane in the observed z_{850} band at $z < 1$. The left panel shows the location of galaxies which are identified as non-mergers within the Gini- M_{20} plane. The right panel shows the location of galaxies in CA space that are identified as a merger within the Gini- M_{20} plane. As can be seen, many of the Gini- M_{20} mergers would be identified as a non-merger within CAS space.

galaxy mergers (Conselice 2003). This was later calibrated by Conselice (2006) using N-body models of galaxy mergers, where it was found that this condition will identify a merger during 0.3-0.5 Gyr of its evolution. Thus, during the merger process the asymmetry index will only find a major merger in progress for part of the merger, and will not be sensitive to minor mergers which have mass ratios of 1:5 and greater (Conselice 2006).

On the other hand, mergers in Gini/ M_{20} are defined by Lotz et al. (2006) to be systems which meet the criteria,

$$G > -0.115 \times M_{20} + 0.384. \quad (6)$$

The first test of the merger method is to see how galaxies identified within the CAS and Gini/ M_{20} methods compare. First, we show in Figure 8 where galaxies identified as mergers with the CAS merger criteria (eq. 5) would fall on the Gini- M_{20} digram. We also show on Figure 9 all galaxies above the Gini/ M_{20} limit for mergers (eq. 6) re-plotted on the concentration vs. asymmetry diagram. We do this to determine if the galaxies which would be identified as a merger within the Gini/ M_{20} space are the same as those in the merger category in CAS space, and vice-versa. We can conclude from these figures that almost all galaxies above the CAS limit would be identified as a merger within the Gini/ M_{20} plane (Figure 8), but the reverse is not necessarily true.

As Figure 9 shows, almost all galaxies identified as non-mergers in the Gini/ M_{20} space are located in the normal galaxy region of CAS space. However, when we examine the location of galaxies identified as mergers within the Gini/ M_{20} space, and replot them on the CAS space, we find that these galaxies occupy a large volume of this space.

There are many systems which fall into the $A > 0.35$ region, but the majority of galaxies are within the region of CAS space where normal galaxies are expected. What this means is that either the Gini/ M_{20} criteria is not locating true mergers, or that it is much more sensitive to various merger phases and time-scales than the CAS indices.

5 THE MERGER HISTORY UP TO $Z \sim 3$

5.1 Redshift and Morphological K-Corrections

5.1.1 Signal to Noise Reduction in CAS parameters

A very important issue that we must address in this study, which compares properties of galaxies at different redshifts, is the fact that measured parameters, as well as the detection of galaxies themselves, can change solely due to the result of redshift and distant effects. The rapidly increasing luminosity distance of galaxies, with the correspondingly slowly changing angular size distance, produces a $(1+z)^4$ decline in surface brightness. Although within the UDF we are easily detecting all galaxies down to our mass limits (Conselice et al. 2003a), changes in the signal-to-noise ratio (S/N) and resolution due to redshift can mask, or mimic, real evolution in structural parameters (Conselice 2003; Conselice et al. 2003a). We address these issues using simulations and apply this information to correct our asymmetry measurements, and constrain possible evolution.

Two types of simulations were performed, those on nearby galaxies placed at high redshifts (Conselice 2003), and by simulating galaxies imaged at $z \sim 0.5$ placed at higher redshifts (see also Conselice et al. 2003a). First, we

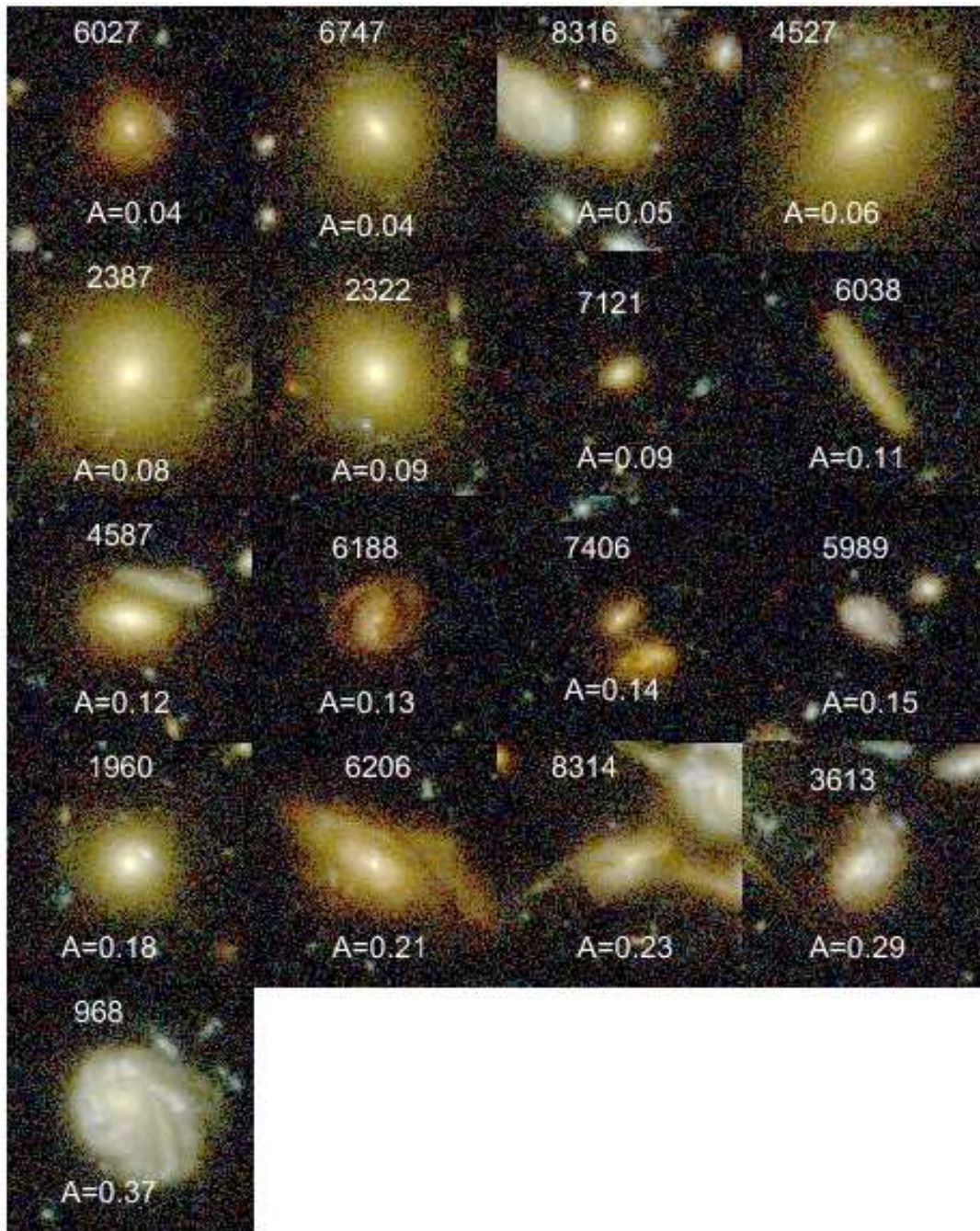


Figure 10. Colour images of galaxies with stellar masses $M_* > 10^{10} M_\odot$ at redshifts $0.5 < z < 1.2$ in the Hubble Ultra Deep Field. Plotted on the top of each images is the ID number from Coe et al. (2006), and the bottom number is the computed value of the asymmetry index in the B-band (A_B).

carried out simulations to determine how galaxy structures change by using galaxies within the lowest redshift bin around $z \sim 0.5$, and which have $M_B < -18$, roughly the limit of our mass sample with $M_* > 10^8 M_\odot$.

The images of these objects in their rest-frame B-band morphology are simulated as they would appear at various redshifts from $z = 1$ to 3. These simulations were done by creating a new background for these galaxies with the same noise characteristics as the real data, then randomly placing the simulated galaxies into these backgrounds. The galaxies are reduced in resolution, signal to noise, flux, and surface

brightness, and convolved with the PSF (see also Conselice et al. 2003a).

The result of all of these simulations is that the measured values of the asymmetries, and the other CAS parameters, become lower at higher redshifts (see also Conselice et al. 2003a; Conselice 2003). The average corrections necessary for these effects are generally low, with differences $\delta A = 0.04 - 0.06$ for the redshift ranges studied in this paper.

Furthermore, we find a very slight difference in retrieved asymmetries for fainter vs. brighter galaxies with different

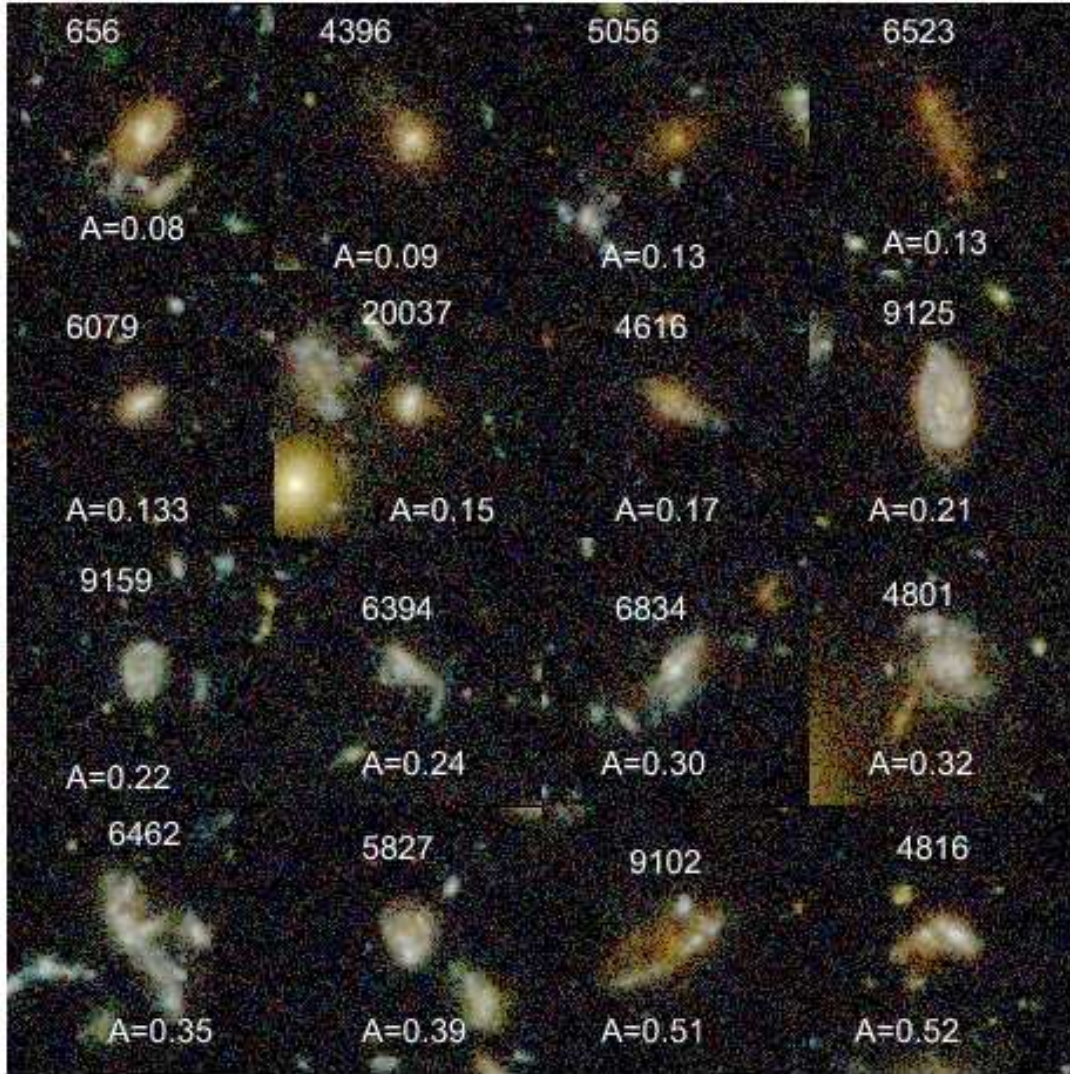


Figure 11. Galaxies with stellar masses $M_* > 10^{10} M_\odot$ at redshifts $1.2 < z < 1.6$. Plotted on the top of each images is the ID number from Coe et al. (2006), and the bottom number is the computed value of the asymmetry index in the B-band (A_B).

magnitudes in each redshift range. We find that the fainter galaxies are generally affected by noise more than brighter ones, and hence the systematics effects (and corrections) are larger, by roughly $\delta A \sim 0.02$, on average. As this is usually smaller than the random measurement errors for these faint galaxies, we do not account for this small difference. As discussed in Conselice et al. (2000a), where similar simulations are done in terms of absolute S/N and resolution, the asymmetry index is not greatly affected by the reduced resolution and lower S/N for $z < 3$ galaxies with $M_B < -18$ within the UDF.

5.1.2 Quantitative Morphological K-Correction

The above corrections are however for galaxies affected just by signal to noise and resolution due to redshift, assuming that the structure of the galaxy is inherently the same. However, in our study we are examining galaxies in the observed z_{850} band, which corresponds to various rest-frame wave-

lengths at different redshifts (Figure 3). This results in the observed z_{850} -band probing bluer light at higher redshifts.

We can account for this change using the results from §4.2, where we calculate changes in the CAS and Gini/ M_{20} parameters at $z < 1.25$. At these redshifts we are probing with the ACS filters the rest-frame optical and rest-frame UV for the same systems, allowing us to compare how indices change at shorter wavelengths probed with ACS at higher redshift. Table 1 tabulates the change in the CAS Gini/ M_{20} parameters as a function of redshift. Using this table, we can calculate the average off-set between the rest-frame observed values and those at rest-frame B-band ($\sim 0.45 \mu\text{m}$). This change in parameters with wavelength is a function of galaxy type. Thus, we can correct the CAS values to their rest-frame B-band values depending on their eye-ball estimates of morphological type.

For example, at $z \sim 2.5$ the rest-frame wavelength probed by the z_{850} -band is roughly $\lambda_{z\text{-rest}} = 0.32 \mu\text{m}$. Using Table 1 this gives us a changed of $\Delta A = -0.10$ for Pec-

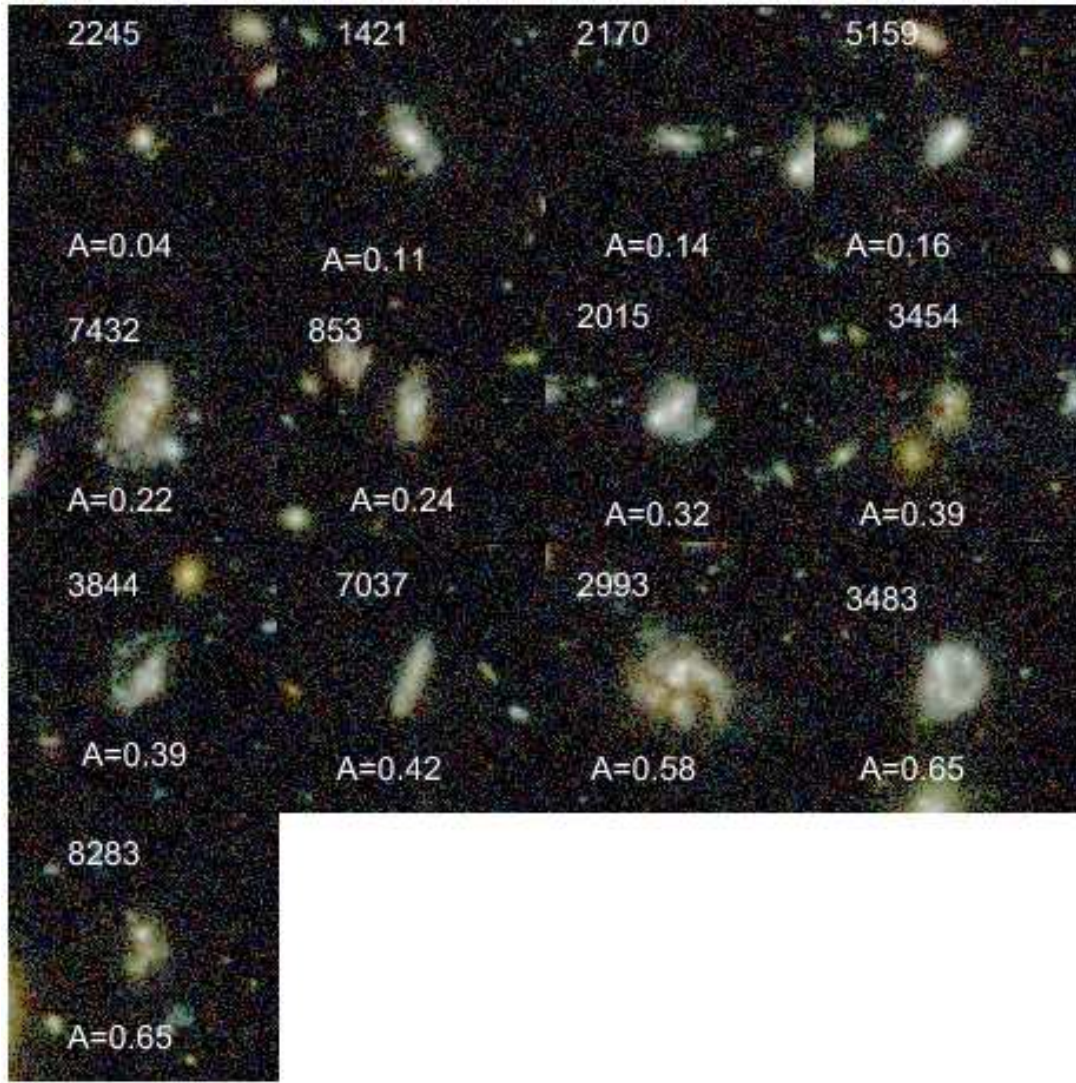


Figure 12. Galaxies with stellar masses $M_* > 10^{10} M_\odot$ at redshifts $1.6 < z < 2.2$. Plotted on the top of each images is the ID number from Coe et al. (2006), and the bottom number is the computed value of the asymmetry index in the B-band (A_B).

liars, -0.06 for spirals and -0.03 for ellipticals, using the $z = 0.75 - 1.25$ results. These changes are slightly different using the $z = 0.25 - 0.75$ values, although the general overall reduction in asymmetry is similar. We apply this correction to each galaxy, depending on its wavelength and morphological type when we compute the merger fraction.

If we denote this morphological k -correction as $\Delta A_{k\text{-corr}}$, and the redshift correction (§5.1.1) as ΔA_z , then the final asymmetry we use for our measurements of the merger fraction is given by

$$A_{B,\text{final}} = A(z_{850}, z, T) + \Delta A_{k\text{-corr}} + \Delta A_z, \quad (7)$$

where the $A_{B,\text{final}}$ is the derived rest-frame B-band morphology of the galaxy under study, and $A(z_{850}, z, T)$ is the observed asymmetry in the z_{850} -band, which is a function of the redshift z , and morphological-type (T). Note that in our case, $\Delta A_{k\text{-corr}} < 0$ and $\Delta A_z > 0$ at $z > 1.5$.

We use these corrections to utilise the CAS definition for finding major-mergers, which requires that $A_B > 0.35$.

As explained in detail in Conselice (2006), there are major-mergers with $A_B < 0.35$, and thus we are not complete in finding mergers by using this definition. However, because this asymmetry limit is well defined, it allows us to determine the time-scale for merging and thus convert the merger fraction measured with the $A_B > 0.35$ limit into a merger rate.

5.2 Visual Appearance of Massive Galaxies

Before we determine the merger history for our sample of galaxies, it is instructive to examine the visual structures of our sample and the corresponding asymmetries of these galaxies. As an example, we examine how the most massive galaxies look as a function of redshift. Figures 10 through 13 show the visual morphologies of galaxies with $M_* > 10^{10} M_\odot$ up to redshifts $z \sim 3$. We plot the final asymmetry values for these galaxies in each of their respective panels. There are a few interesting trends in the apparent structures

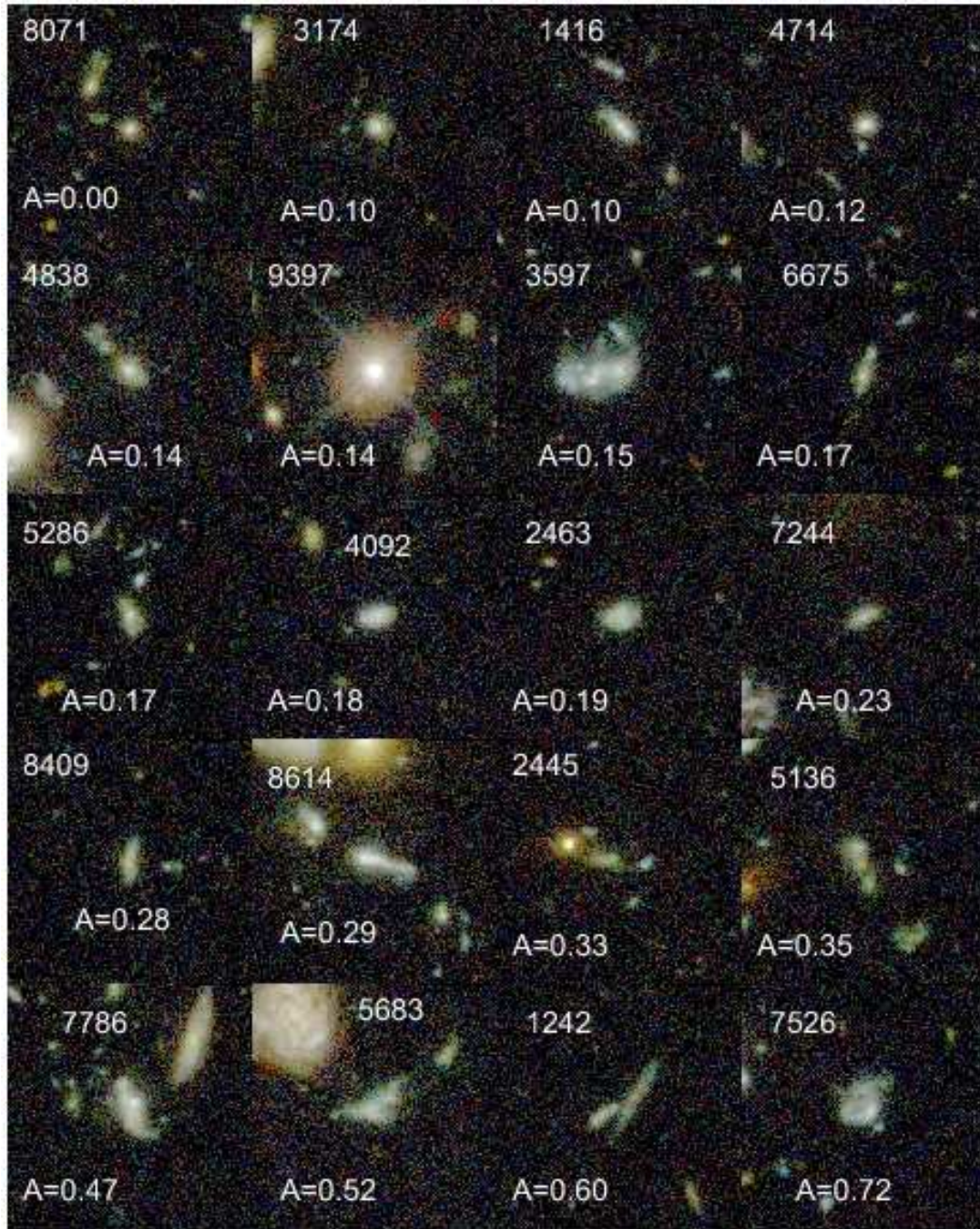


Figure 13. Galaxies with stellar masses $M_* > 10^{10} M_\odot$ at redshifts $2.2 < z < 3$. Plotted on the top of each images is the ID number from Coe et al. (2006), and the bottom number is the computed value of the asymmetry index in the B-band (A_B).

of these galaxies. The first is that in the lowest redshift bin, $0.5 < z < 1.2$ a large fraction of the $M_* > 10^{10} M_\odot$ galaxies have a regular normal elliptical or spheroid-like appearance. This is confirmed by where these galaxies fall in the CAS and Gini/ M_{20} space (e.g., Figure 5; see also Conselice et al. 2007b). As can also be seen, these massive galaxies are generally reddish in appearance, which is also the result when examining galaxy colour and stellar mass (e.g., Bundy et al. 2006).

A few of the galaxies within the range $0.5 < z < 1.2$ appear to be peculiars or spiral galaxies. This is even more the

case when we examine massive galaxies at higher redshifts (Figure 11-13). This change can be seen even more significantly in the $1.2 < z < 1.6$ redshift range. While there are some galaxies at stellar masses $M_* > 10^{10} M_\odot$ which appear to be roughly spherical, and in some cases red (e.g., object 5056, Figure 11), but already the majority of these objects have an appearance which suggests that these galaxies are undergoing some kind of formation either through star formation in a disk or through a merger process of some type. In this redshift range there are a few obvious examples of

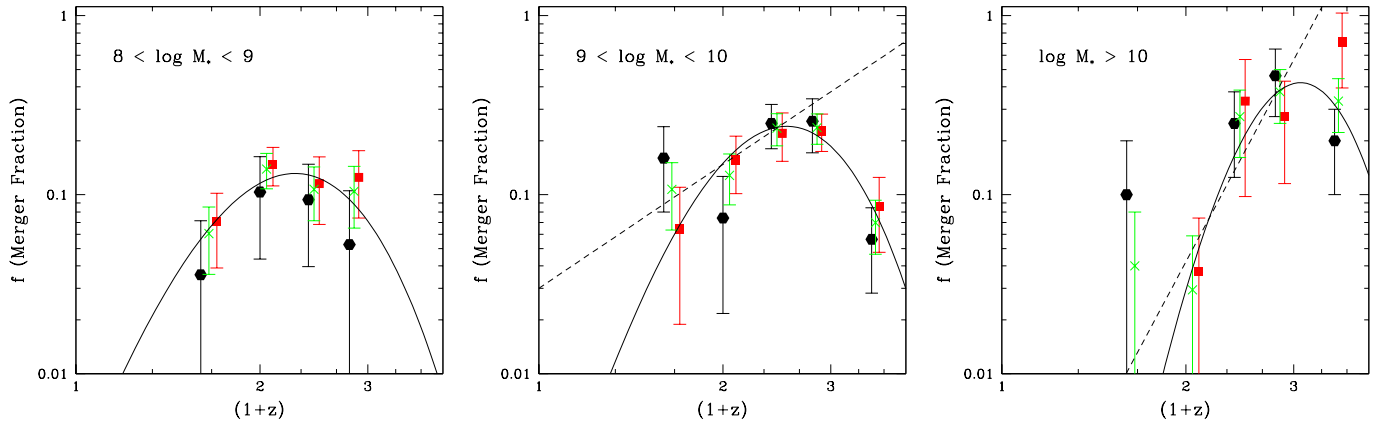


Figure 14. The merger fraction as a function of redshift and stellar mass. Shown are the merger fractions at mass limits of $8 < \log M_* < 9$, $9 < \log M_* < 10$, and $\log M_* > 10$. The black circles show the merger fraction as measured in the UDF, while the red boxes are the merger fractions from the HDF-North where we can probe the rest-frame optical (Conselice et al. 2003a). The green crosses show the evolution of the merger fraction for a combined UDF and HDF-N sample.

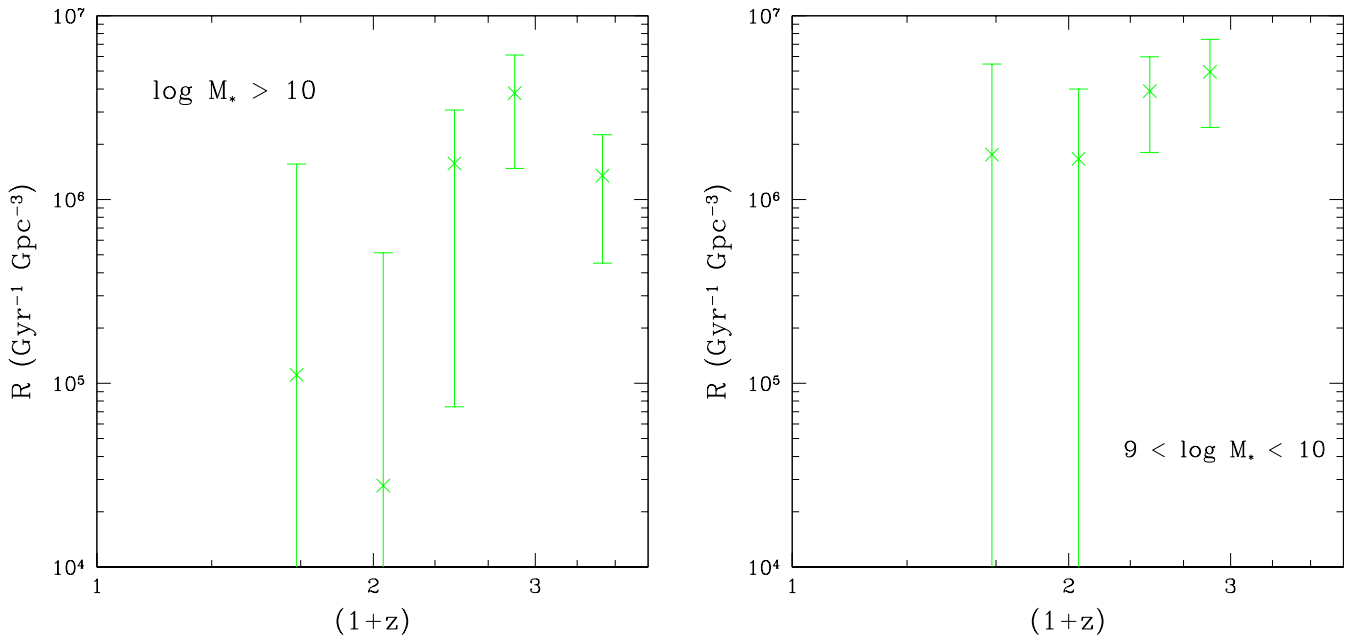


Figure 15. The merger rate in units of $\text{Gyr}^{-1} \text{Gpc}^{-3}$ for the combined UDF and HDF-N samples. The merger rate is given by equation (10) where we include number densities as measured by Drory et al. (2005) and time-scales for CAS mergers from Conselice (2006).

galaxies which are undergoing some type of merger and have resulting high asymmetries (objects 6462, 9102 and 4816).

In the highest redshift ranges $1.6 < z < 2.2$ (Figure 12) and $2.2 < z < 3.0$ (Figure 13) there are more irregular/merging galaxies. There are however interesting exceptions to this. In Figure 12 and 13 there are cases of galaxies which look normal, and are perhaps morphological progenitors of elliptical galaxies (e.g., objects 2245, 8071, 3174). There are also examples of galaxies at these redshift ranges which have a disk like appearance (e.g., objects 1421, 2170, and 5159). Clearly, as discussed within the Hubble Deep Field, there is a diversity of morphologies for the most massive galaxies even at $z > 2$ (Conselice et al. 2003a). This

might be the result of these galaxies undergoing an inhomogeneous formation history with some galaxies undergoing merging, and others in a more quiescent state. In the next section we investigate merger fractions based on these structural appearances and their measured CAS parameters.

5.3 Merger Fractions

One of the major questions in extragalactic studies is the role of mergers in the formation of galaxies. There are various types of mergers - minor and major, and the relative role of these over cosmic time is largely unknown. One of the great benefits of using the CAS system for finding mergers

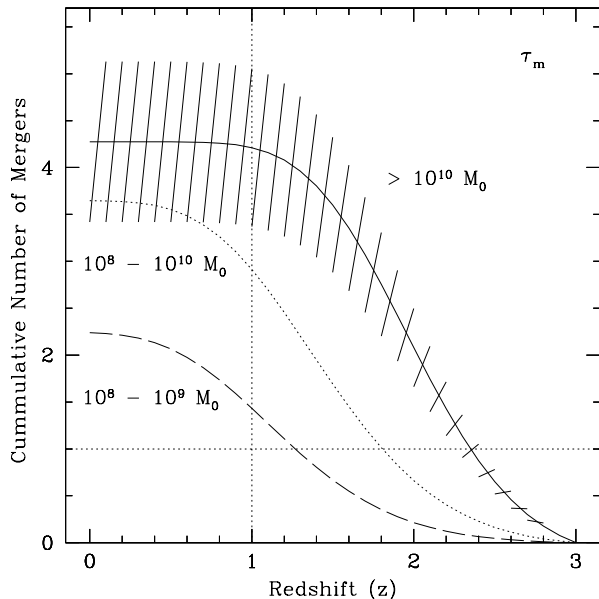


Figure 16. The cumulative number of major mergers for galaxies of various masses as a function of redshift. These cumulative mergers beginning at $z = 3$. The error range for the $M_* > 10^{10} M_\odot$ galaxies is shown. In total, the most massive galaxies have a larger number of total galaxy mergers than the lower mass systems.

is that it allows us to quantify the merger fraction, merger rates, and thus the number of mergers occurring in a galaxy population (Conselice et al. 2003a; Conselice 2006). While in this section we investigate the merger fractions based on standard techniques we have developed (e.g., Conselice 2003; Conselice 2006; Bridge et al. 2007), we examine in detail those galaxies that we consider mergers later in a future paper in this series.

The first observation we can derive from our CAS values is the evolution of the merger fraction. We determine the merger fraction for galaxies of various masses using the criteria from equation (5). There are a few caveats to measuring the merger fraction which we must consider before using these values to determine how galaxies are evolving due to major mergers, or even to measure the merger fraction. Our final merger fraction values are tabulated in Table 2.

First, it is important to note that the merger fraction we measure is in no sense the total galaxy merger fraction. All merger fractions we derive are computed using a certain technique, in this case the CAS parameters, and this technique is only sensitive to a well defined time-range. In the case of CAS mergers, this time-span is roughly 0.4 Gyr (Conselice 2006). As determined in Conselice (2006) there are phases of a merger which will not be picked up by the CAS technique. A different technique will find a different merger fraction if it has a time sensitivity different from the CAS system. For example galaxy pair methods have roughly a

factor of two different time-scale for a merger than the CAS system (De Propris et al. 2007), but gives the same merger rate. We therefore expect galaxies that by eye appear as a merger, but will not have a high asymmetry.

There are a few ways to fit the merger fraction. The first is the traditional power-law format (Patton et al. 2002; Conselice et al. 2003; Bridge et al. 2007). This fitting format is given by,

$$f_m(z) = f_0 \times (1 + z)^m \quad (8)$$

where $f_m(z)$ is the merger fraction at a given redshift, f_0 is the merger fraction at $z = 0$, and m is the power-law index for characterising the merger fraction evolution.

Another way to characterise the merger fraction evolution which dates back to theoretical arguments based on Press-Schechter formalism for merging (Carlberg 1990) is a combined power-law exponential evolution. This form appears to be a better fit to all of the redshift data than a simple power-law (Conselice 2006). The formula for this evolution is given by:

$$f_m = \alpha(1 + z)^m \times \exp(\beta(1 + z)), \quad (9)$$

where the $z = 0$ merger fraction is given by $f_m(0) = \alpha \times \exp(\beta)$.

We plot in Figure 14 the merger fraction for the sample of galaxies in the UDF as well as the HDF-N, where there is NICMOS high-resolution imaging of galaxies, and thus the merger fraction can be measured strictly in the rest-frame optical at all redshifts. The results derived within both fields are however very similar. We show the combined HDF-N and UDF merger fractions as the green crosses on Figure 14. The merger fractions for the UDF are always measured in the observed z_{850} -band. We however correct for both the effects of redshift, as well as for the morphological k -correction using the rest-frame B-band asymmetry calculated using equation (7).

We show as the solid line on Figure 14 the best fit values for the merger fraction using the combined exponential/power-law fitting formula (eq. 9). We also fit up to the merger fraction redshift peak the power-law form given by equation (8) for all but the $10^8 M_\odot < M_* < 10^9 M_\odot$ galaxies where there are too few points to carry out a reliable fit. The values found for the $M_* > 10^{10} M_\odot$ galaxies are: $\alpha = 0.01 \pm 0.02$, $m = 33 \pm 16$, and $\beta = -10 \pm 5$ for the exponential/power-law formalism. The lower mass systems have a systematically higher value of α , a lower value of m , and a larger (less negative) value of β .

The peak merger fraction within the exponential/power-law fit occurs at a redshift of $z_{\text{peak}} = -(1 + m/\beta)$. Using our fits, we calculate that the peak in the merger fraction occurs at redshifts $z_{\text{peak}} = 2.08$ for galaxies with $M_* > 10^{10} M_\odot$, and $z_{\text{peak}} = 1.54$, and $z_{\text{peak}} = 1.28$ for galaxies with $10^9 M_\odot < M_* < 10^{10} M_\odot$ and $10^8 M_\odot < M_* < 10^9 M_\odot$ selected galaxies, respectively. This suggests that the peak merger fraction appears to occur later for lower-mass galaxies. The downsizing for the lower-mass galaxies therefore might occur because these systems are not merging as quickly as the higher mass galaxies.

Table 2. Merger fractions as a function of stellar mass and redshift

z (UDF)	f($10^8 M_{\odot} - 10^9 M_{\odot}$)	f($10^9 M_{\odot} - 10^{10} M_{\odot}$)	f(> $10^{10} M_{\odot}$)
0.6	0.04±0.04	0.16±0.08	0.10±0.10
1.0	0.10±0.06	0.07±0.05	0.00±0.00
1.4	0.09±0.05	0.25±0.07	0.25±0.13
1.8	0.06±0.05	0.26±0.09	0.46±0.19
2.5	...	0.06±0.03	0.20±0.10
z (HDF)	f($10^8 M_{\odot} - 10^9 M_{\odot}$)	f($10^9 M_{\odot} - 10^{10} M_{\odot}$)	f(> $10^{10} M_{\odot}$)
0.6	0.07±0.03	0.06±0.05	0.00±0.00
1.0	0.15±0.04	0.16±0.06	0.04±0.04
1.4	0.12±0.05	0.22±0.07	0.33±0.24
1.8	0.13±0.05	0.23±0.05	0.27±0.16
2.5	...	0.09±0.04	0.71±0.32
z (Combined)	f($10^8 M_{\odot} - 10^9 M_{\odot}$)	f($10^9 M_{\odot} - 10^{10} M_{\odot}$)	f(> $10^{10} M_{\odot}$)
0.6	0.06±0.02	0.11±0.04	0.04±0.04
1.0	0.14±0.03	0.13±0.04	0.03±0.03
1.4	0.11±0.04	0.24±0.05	0.27±0.11
1.8	0.10±0.04	0.24±0.05	0.38±0.13
2.5	...	0.07±0.02	0.33±0.11

5.4 Merger Rates and the Cumulative Number of Mergers

5.4.1 The Galaxy Merger Rate at $z < 3$

By using the number densities for galaxies within our mass ranges from previous work, and the time-scales from our CAS method, we can calculate the merger rate for our $M_* > 10^8 M_{\odot}$ galaxy samples. The number densities for our systems are taken from Drory et al. (2005), and the time-scales for merging are derived from equation 10 in Conselice (2006), based on N-body models analysed using CAS indices.

The galaxy merger rate for our systems can be calculated through the merger rate equation,

$$\mathfrak{R}(z) = f_{\text{gm}}(z) \cdot \tau_{\text{m}}^{-1} n_{\text{gm}}(z) \quad (10)$$

where n_{gm} is the number densities of galaxies within a given stellar mass range, and f_{gm} is the galaxy merger fraction. Note that this is not the merger fraction, which is the number of mergers divided by the number of galaxies, which is roughly half the galaxy merger fraction (Conselice 2006). We convert our merger fractions used earlier in this paper to galaxy merger fractions using the relation,

$$f_{\text{gm}} = \frac{2 \times f_{\text{m}}}{1 + 1/f_{\text{m}}}. \quad (11)$$

The time-scales we use in eq. (10) (τ_{m}) come from the calculations based on N-body models in Conselice (2006). There is a slight decrease in the time-scale for galaxies with lower masses. We utilise these results to calculate that the merger time-scale for the most massive galaxies with $M_* > 10^{10} M_{\odot}$ is $\tau_{\text{m}} = 0.34$ Gyr, and slightly lower, between 0.27-0.29 Gyr for the lower mass systems.

By utilising the number densities for galaxies of a given stellar mass from Drory et al. (2005), the time-scales from Conselice (2006), and the galaxy merger fractions from this paper, we compute the merger rate as a function of stellar mass using equation (10). The results of this calculation are shown in Figure 15. As can be seen, the merger

rate decreases at lower redshifts for galaxies at masses $10^9 M_{\odot} < M_* < 10^{10} M_{\odot}$, with the average merger rate, $\langle \mathfrak{R} \rangle \sim 3 \times 10^6$ galaxies merging $\text{Gyr}^{-1} \text{Gpc}^{-3}$.

The more massive galaxies with $M_* > 10^{10} M_{\odot}$ have a lower merger rate at all redshifts, and a more steeply declining merger rate with time. We find that the merger rate declines as $\sim (1+z)^{5.5 \pm 2.5}$ for these massive galaxies, which is similar to the decline in the merger fraction. The merger rate for $10^9 M_{\odot} < M_* < 10^{10} M_{\odot}$ galaxies evolves as $\sim (1+z)^{2.6 \pm 0.6}$, again similar to the evolution in the merger fraction, and showing a more gradual decline with time compared to more massive galaxies. The steeper decline in the merger rate for more massive galaxies is likely partially the reason the star formation rate in these systems also drops much faster than for lower mass systems (Conselice et al. 2007b).

5.4.2 Total Number of Mergers at $z < 3$

One of the major benefits to calculating the merger rate is that it allows us to determine the total number of major mergers a galaxy of a given mass will undergo between two redshifts. We calculate the total number of major mergers a galaxy with $M_* > 10^{10} M_{\odot}$ undergoes from $z \sim 3$ to $z \sim 0$ using equation (11) in Conselice (2006). We use our fitted exponential/power-law functions for this calculation, which has an associated uncertainty associated with with the fit.

Figure 16 shows the cumulative number of mergers which have occurred from $z \sim 3$ to $z \sim 0$ as a function of mass. Although we do not have a good idea of the merger fraction or rate for our massive galaxies at $z < 0.6$, we know from previous work that the merger fractions for these systems is very low, particularly for the most massive galaxies (e.g., Patton et al. 2002; De Propris et al. 2007; Conselice et al. 2007b). Using our merger fraction fits, we calculate that the average number of mergers a galaxy with $M_* > 10^{10} M_{\odot}$ will undergo from $z \sim 3$ to 0 is $N_{\text{m}} = 4.3_{-0.8}^{+0.8}$. This is nearly the same as the value we obtained by using the HDF-

N, where for the same mass range, we found $N_m = 4.4_{-0.9}^{+1.1}$ (Conselice 2006). The uncertainties in this calculation are dominated by those from the merger-time scale calculation.

The lower mass galaxies generally have a lower total number of major mergers occurring at $z < 3$ (Figure 16). This is perhaps partially because we cannot measure the merger fraction for these lower mass galaxies reliably at $z < 0.5$. The volume probed by the UDF is not large enough to reliably trace this merger fraction, and other fields which are large enough, are not deep enough. In general however, it appears that the lower mass galaxies do not undergo the same number of major mergers as the highest mass galaxies. Furthermore, it appears, as we discussed in Conselice (2006), that most of the major mergers for the most massive galaxies occurs at higher redshifts, $z > 1$, although for the lower mass galaxies there is still some merging at these later times. This is consistent with the downsizing of star formation (e.g., Bundy et al. 2006) produced through merging, and the fact that peculiar galaxies found at lower redshifts often contain a lower stellar mass (e.g., Bundy et al. 2005).

6 SUMMARY

This paper begins a series in which we examine the structures of distant galaxies, and determine the likely role of galaxy merging in the formation of galaxies. In this paper we examine structural parameters using the CAS and Gini/M₂₀ system on galaxies found within the Hubble Ultra Deep Field (UDF). We also examine the stellar masses and eye-ball estimates of morphological types for these systems. Our major conclusions and findings include:

I. Down to $z_{850} = 27$ the majority of galaxies found in the UDF are peculiar in appearance. This suggests that galaxy formation is actively ongoing for these systems.

II. We compare how visual estimates of morphology agree with positions in CAS and Gini/M₂₀ space. We find a generally good agreement between these methods with the merger region in CAS space nearly totally occupied by galaxies which are visually classified as peculiars/mergers.

III. We examine the merger fraction of galaxies in the UDF using the CAS system and compare with our previous results of the merger fraction and rate derived using the Hubble Deep Field. We confirm our earlier measurements of the merger history, including the fact that the highest mass galaxies with $M_* > 10^{10} M_\odot$ have a steeply increasing merger fraction up to $z \sim 3$. This increase can be fit as a power-law $\alpha(1+z)^m$, with $m \sim 6$ for the combined UDF and HDF-N sample. We find that the merger fraction for lower mass galaxies are lower at high redshift, but reach their peak fractions at lower redshifts. In total we find that $M_* > 10^{10} M_\odot$ galaxies undergo on average $4.3_{-0.8}^{+0.8}$ major mergers at $0 < z < 3$, with most of this merging occurring at $z > 1$.

We thank Dan Coe for making his analysis results of the UDF freely available, and Kevin Bundy for assistance with the stellar masses. We also acknowledge support from the University of Nottingham.

REFERENCES

- Abraham, R., van den Bergh, S., Nair, P. 2003, ApJ, 588, 218
- Benitez, N. 2000, ApJ, 536, 571
- Beckwith, S., et al. 2006, AJ, 132, 1729
- Bershady, M.A., Jangren, J.A., Conselice, C.J. 2000, AJ, 119, 2645
- Bridge, C., et al. 2006, ApJ, 659, 931
- Bruzual, G., Charlot, S. 2003, MNRAS, 344, 1000
- Bundy, K., et al. 2006, ApJ, 651, 120
- Bundy, K., Ellis, R.S., Conselice, C.J. 2005, ApJ, 625, 621
- Carlberg, R. 1990, ApJ, 359, 1L
- Cassata, P., et al. 2005, MNRAS, 357, 903
- Coe, D., Benitez, N., Sanchez, S.F., Jee, M., Bouwens, R., Ford, H. 2006, AJ, 132, 926
- Conselice, C.J. 1997, PASP, 109, 1251
- Conselice, C.J., Bershady, M.A., Jangren, A. 2000a, ApJ, 529, 886
- Conselice, C.J., Bershady, M.A., Gallagher, J.S. 2000b, A&A, 354, 21L
- Conselice, C.J., Gallagher, J.S., Calzetti, D., Homeier, N., Kinney, A. 2000c, AJ, 119, 79
- Conselice, C.J. 2003, ApJS, 147, 1
- Conselice, C.J., Bershady, M.A., Dickinson, M., Papovich, C. 2003a, AJ, 126, 1183
- Conselice, C.J., Chapman, S.C., Windhorst, R.A. 2003b, ApJ, 596, 5L
- Conselice, C.J., Gallagher, J.S., Wyse, R.F.G. 2002, AJ, 123, 2246
- Conselice, C.J., et al. 2004, ApJ, 600, 139L
- Conselice, C.J., Blackburne, J., Papovich, C. 2005a, ApJ, 620, 564
- Conselice, C.J., Bundy, K., Ellis, R., Brichmann, J., Vogt, N., Phillips, A. 2005b, ApJ, 628, 160
- Conselice, C.J. 2006a, MNRAS, 373, 1389
- Conselice, C.J. 2006b, ApJ, 638, 686
- Conselice, C.J., et al. 2007a, ApJ, 660, 55L
- Conselice, C.J., et al. 2007b, MNRAS, in press, arXiv:0708.1040
- Courteau, S., McDonald, M., Widrow, L.M., Holtzman, J. 2007, ApJ, 655, 21
- De Propriis, R., Conselice, C.J., Driver, S.P., Liske, J., Patton, D., Graham, A., Allen, P. 2007, preprint, arXiv:0705.2528
- Dickinson, M., et al. 2000, ApJ, 531, 624
- Driver, S., et al. 1998, ApJ, 496, 93L
- Drory, N., et al. 2005, ApJ, 619, 131L
- Elmegreen, D.M., Elmegreen, B.G., Rubin, D.S., Schaffer, M.A. 2005, ApJ, 631, 85
- Faber, S.M., et al. 2007, ApJ, 665, 265
- Giavalisco, M., et al. 2004, ApJ, 600, 93L
- Glazebrook, K., Ellis, R., Santiago, B., Griffiths, R. 1995, MNRAS, 275, 19L
- Grogin, N.A., et al. 2005, ApJ, 627, 97L
- Hernandez-Toledo, H.M., Avila-Reese, V., Conselice, C.J., Puerari, I. AJ, 2005, AJ, 129, 682
- Hibbard, J.E., & Vacca, W.D. 1997, AJ, 114, 1741
- Lotz, J.M., Primack, J., Madau, P. 2004, AJ, 128, 163L
- Lotz, J.M., et al. 2006, astro-ph/0602088
- Moustakas, L.A., et al. 2004, ApJ, 600, 131L
- Papovich, C., Dickinson, M., Giavalisco, M., Conselice,

- C.J., Ferguson, H.C. 2005, ApJ, 631, 101
Papovich, C., Giavalisco, M., Dickinson, M. Conselice, C.J.,
Ferguson, H.C. 2003, ApJ, 598, 827
Patton, D.R., et al. 2002, ApJ, 565, 208
Ravindranath, S., et al. 2006, ApJ, 652, 963
Stanford, S.A., Dickinson, M.E., Postman, M., Ferguson,
H.C., Lucas, R.A., Conselice, C.J., Budavari, T.,
Somerville, R. 2004, AJ, 127, 131
Taylor-Mager, V., Conselice, C., Windhorst, R., Jansen, R.
2007, ApJ, 659, 162
Teplitz, H.I., et al. 2006, AJ, 132, 853
Thompson, R.I., et al. 2005, AJ, 130, 1
Trujillo, I., Conselice, C.J., Bundy, K., Cooper, M.C.,
Eisenhardt, P., Ellis, R.S. 2007, MNRAS, in press,
arXiv:0709.0621
Williams, R., et al. 1996, AJ, 112, 1335
Windhorst, R., et al. 2002, ApJS, 143, 113
Wright, S.A., et al. 2007, ApJ, 658, 78